www.mtri.org

Evaluating the Use of Unmanned Aerial Vehicles for Transportation Purposes

Final Report, No. RC-1616

Prepared by:

Colin Brooks[1], Richard J. Dobson[1], David M. Banach[1], David Dean[1], Thomas Oommen[2], Rudiger Escobar Wolf[2], Timothy C. Havens[2], Theresa M. Ahlborn[2], Ben Hart[1]

[1] Michigan Tech Research Institute, 3600 Green Ct., Ste. 100, Ann Arbor, Michigan 48105
[2] Michigan Technological University, 1400 Townsend Dr., Houghton, Michigan, 49931

Program Manager:

Steven J. Cook, P.E.
Michigan Department of Transportation
6333 Lansing Road
Lansing, MI 48917

Research Manager:

André Clover, P.E.
Michigan Department of Transportation
8885 Ricks Road
Lansing, MI 48917

Revised version of April 7, 2015

1. Report No. RC-1616	**2. Government Accession No.**	**3. MDOT Project Manager** Steven J. Cook, P.E.
4. Title and Subtitle Evaluating the Use of Unmanned Aerial Vehicles for Transportation Purposes		**5. Report Date** 3/27/2015 **6. Performing Organization Code** 38-6005955
7. Author(s) C.Brooks, R.Dobson, D.Banach, D. Dean, T.Oommen, R.Wolf, T.Havens, T. Ahlborn, B.Hart		**8. Performing Org. Report No.** MTRI-MDOTUAV-FR-2014
9. Performing Organization Name and Address Michigan Technological University 1400 Townsend Drive Houghton, MI 49931		**10. Work Unit No. (TRAIS)** **11. Contract No.** 2013-067 **11(a). Authorization No.** Auth. No 1
12. Sponsoring Agency Name and Address Michigan Department of Transportation Office of Research and Best Practices 425 West Ottawa Street Lansing MI 48933		**13. Type of Report & Period Covered** Final Report **14. Sponsoring Agency Code**
15. Supplementary Notes		

16. Abstract

Advances in unmanned aerial vehicle (UAV) technology have enabled these tools to become easier to use and afford. In a budget-limited environment, these flexible remote sensing technologies can help address transportation agency needs in operations, maintenance, and asset management while increasing safety and decreasing cost. This project tested and evaluated five main UAV platforms with a combination of optical, thermal, and LiDAR sensors to assess critical transportation infrastructure and issues such as bridges, confined spaces, traffic flow, and roadway assets. A State of the Practice report was completed, and a series of lab testing were accomplished to ensure practicality and safe operations. Field demonstrations were completed at bridges, pump stations, and conferences. The project team gave a series of technical demonstrations at the Intelligent Transportation Systems World Congress in Detroit in September, 2014, enabling outreach to a wide domestic and international audience who gained understanding of the advanced research that MDOT is funding. These demonstrations showed that UAV technologies provide many advantages to helping MDOT cost-effectively assess, manage, and maintain its resources, providing benefit to staff and the traveling public.

17. Key Words Unmanned aerial vehicle, UAV, transportation, operations, maintenance, asset management, bridges, traffic, confined spaces, GIS, remote sensing		**18. Distribution Statement** No restrictions. This document is available to the public through the Michigan Department of Transportation.	
19. Security Classification - report Unclassified	**20. Security Classification - page** Unclassified	**21. No. of Pages** 201	**22. Price**

Acknowledgments

The project team would like to thank and acknowledge the program manager, Steve Cook, and the research manager, André Clover, for their advice and oversight during this project. The PI would like to thank his project team for their dedication to collecting quality, useful data safely. The help of MDOT staff in accessing and collecting data at field sites, including the pump stations and I-96 Fix construction site near Detroit, was critical to the project and their help is greatly appreciated.

Research Report Disclaimer

"This publication is disseminated in the interest of information exchange. The Michigan Department of Transportation (hereinafter referred to as MDOT) expressly disclaims any liability, of any kind, or for any reason, that might otherwise arise out of any use of this publication or the information or data provided in the publication. MDOT further disclaims any responsibility for typographical errors or accuracy of the information provided or contained within this information. MDOT makes no warranties or representations whatsoever regarding the quality, content, completeness, suitability, adequacy, sequence, accuracy or timeliness of the information and data provided, or that the contents represent standards, specifications, or regulations."

Table of Contents

Table of Contents iii
List of Figures iv
List of Tables x
1. Introduction 1
1.1 Executive Summary 1
1.2 Hypothesis, Objectives, and Scope 4
1.3 State of the Practice for Remote Sensing of Transportation Infrastructure Using Unmanned Aerial Vehicles (UAV) 4
2. UAV Platforms – Technology Overview 5
2.1 Aerial Equipment 5
2.1.2 Blimp 13
2.2 Sensors 17
3. Methodology 32
3.1 Transportation Infrastructure 32
3.2 Lab Testing 43
4. Field Demonstrations & Results 67
4.1 Bridge Inspection – I-96 Fix bridges 67
4.2 Confined Space - Pump Stations and Culverts 85
4.3 Traffic Monitoring 91
4.4 ITS World Congress 92
5. Procedures 104
5.1 Bridge Deck Condition Multi-source Data Evaluation 104
6. Implementation Action Plan 111
6.1 Required Sections 111
6.2 Follow-on ideas 118
7. Conclusions and Recommendations 137
8. References 139
9. Appendices A-1
9.1 List of Acronyms, Abbreviations and Symbols A-1
9.2 State of the Practice for Remote Sensing of Transportation Infrastructure Using Unmanned Aerial Vehicles (UAV) A-2
9.3 Comparison of uncalibrated Digital Number output from Tau 2 with calibrated temperature data from the SC640 cameras A-46

List of Figures

Figure 1.1 A: A Bergen hexacopter, used in the project to collect optical, thermal, and LiDAR data for assessing bridge condition, roadway assets, and other transportation assets. Left – collecting bridge condition data; Right – close-up view. 2
Figure 2.1.1.1 A: Bergen Hexacopter 6
Figure 2.1.1.1 B: Close up of a Nikon D800 mounted to the gimbal under the hexacopter. 7
Figure 2.1.1.2 A: The DJI Phantom Vision 2 small quadcopter UAV 8
Figure 2.1.1.2 B: An example DJI Phantom 2 collected JPEG image with lens correction, of part of the closed stretch of I-96 in Livonia, MI. These types of quick aerial photos can be useful for construction site monitoring and imaging transportation assets and traffic conditions. 9
Figure 2.1.1.3 A: MTRI Blackout Mini H Quad 10
Figure 2.1.1.3 B: Blackout Mini H Quad flying inside a culvert. 10
Figure 2.1.1.4 A: FPVfactory Mariner Waterproof Quad 11
Figure 2.1.1.4 B: Underside of a Belle Isle Bridge taken using the Mariner Waterproof Quadcopter 12
Figure 2.1.1.5 A: Heli-Max 1 Si micro-UAV 12
Figure 2.1.1.5 B: Walkera QR 100S 13
Figure 2.1.2 A: The MTRI blimp being readied for a test flight. Note the camera mounted on a 3 axis gimbal under the blimp. 14
Figure 2.1.2 B: A 35 meters cubed Allsopp Helikite in flight. This image illustrates the airfoil and keel that stabilize and provide some lift to the aerostat. 14
Figure 2.1.2 C: The MTRI blimp being launched for a test flight. The gimbal and camera are visible under the blimp. 15
Figure 2.1.2 D: The gimbal and camera assembly under the blimp. The battery on top of the gimbal supplies power to the gimbal. 16
Figure 2.1.2 E: Ben Hart from MTRI (R) and Andre Clover from MDOT viewing the video feed from the blimp camera on a rugged tablet during testing at MTRI. 16
Figure 2.2.1 A: Example of a Nikon D800 mounted below a Bergen Tazer 800 single rotor UAV ready for deployment. 18
Figure 2.2.1 B: Crazyflie Nano (3.5 inches across and weighs 19 grams) with a keychain camera mounted on top. 19
Figure 2.2.1 C: An example of how stereoscopic imagery for generating 3-D models is collected (Jenson 2007) 20
Figure 2.2.1 D: Bundle adjustment seeks to solve the geometry between photos and to generate 3-D point clouds. This figure shows the relationship between four images that is solved by the bundle adjustment (Wester - Ebbinghaus 1988) 20
Figure 2.2.2 A: A - Spectral radiance as a function of wavelength according to Planck's law. The three curves represent surfaces at different temperatures. The upper extreme of part A also shows the classification of different regions of the electromagnetic spectrum, including the long-wavelength or thermal infrared region, on which most thermal remote sensing instruments work, including the forward looking infrared (FLIR) Tau 2 sensor discussed later. B -Typical atmospheric transmittance through a whole vertical atmospheric column (adapted from Loubere, 2012) for the same wavelengths shown in panel A. Notice the "thermal window" between 8 and 14 micrometers

coinciding with the thermal infrared part of the spectrum, and for which the atmospheric transmittance is high, allowing electromagnetic radiation to travel without much absorption. C - Spectral radiance transmitted through the atmosphere considering the transmittance shown in panel B. 23
Figure 2.2.3 A: Ascending Technologies Pelican. 25
Figure 2.2.3 B: Wallace et al. (2012) forest inventory optocopter platform. 26
Figure 2.2.3 C: An example point cloud produced by Wallace et al. (2012). 26
Figure 2.2.3 D: Primary sensors: LiDAR (center, with yellow sticker), VectorNAV inertial navigation sensor (center, red), Point Grey camera (right). 27
Figure 2.2.3 E: Top view of the primary sensors – LiDAR (silver top) and INS (red) in center; camera at right. 27
Figure 2.2.3 F: Nvidia Jetson embedded computer system enclosure (black) on rear of hexacopter UAV. 29
Figure 2.2.3 G: Power Connections. 30
Figure 3.1.1 A: 3DOBS vehicle mount in the bed of a pickup truck. 33
Figure 3.1.1 B: Cross section illustration of heat flow through solid (left side) and delaminated (right) concrete. For a concrete body heated from its surface (e.g. through solar radiation) the heat flow will start to move away from the surface and through the body's interior. In the presence of a delamination the heat flow is interrupted or slowed down, leading to an increase of temperature right above the delamination. 35
Figure 3.1.2 A: Dallas pump station along I-75. 37
Figure 3.1.2 B: Example of a hatch that a UAV would have to fly through. 38
Figure 3.1.3 A: Two views from traffic cameras on I-475 in Toledo, OH, which monitor traffic through a construction zone. 39
Figure 3.1.3 B: Views of US 23 and Plymouth Road (left and center) from the MTRI blimp (altitude approximately 120 feet) during a lab test flight, and construction site traffic monitoring at the Interstate-96 site using a quadcopter (right). 39
Figure 3.1.4 A: Road side asset detection and tracking algorithm flowchart 40
Figure 3.1.4 B: Examples of road side asset detection in imagery. 41
Figure 3.1.4 C: Detection and tracking a No-Parking sign from above from the UAV. 42
Figure 3.1.4 D: Detection and tracking a No Parking warning sign from side view from UAV. 42
Figure 3.2.1 A: Photo taken of the foam board used to determine the restrictions of AgiSoft Photoscan. 43
Figure 3.2.1 B: The resulting AgiSoft Photoscan model. A total of five images were used to generate the model. 44
Figure 3.2.2 A: DJI Phantom testing in a confined space in the lab at MTRI. 45
Figure 3.2.2 B: Extracted frame from the GoPro video captured from the lab testing of the Phantom 1. 45
Figure 3.2.2 C: DJI Phantom flying in a pump station. 46
Figure 3.2.2 D: DJI Phantom flying in a pump station. 47
Figure 3.2.2 E: Extracted frame from the video captured from the DJI Phantom. 47
Figure 3.2.2 F: Test the Heli-Max 1Si in the MTRI Lab. 48
Figure 3.2.2 G: Extracted frame captured by the Heli-Max 1Si during the lab testing. 48

Figure 3.2.2 H: The Blackout Mini H quad being flown through a section of culvert. 49
Figure 3.2.2 I: An extracted frame from the Blackout while flying through a culvert section. This shows the interior wall of the culvert as the UAV was hovering and turning inside the section. 49
Figure 3.2.3 A: Operating gimbal mounted on the blimp. Notice that while the blimp is nose up, the camera is level. 50
Figure 3.2.4 A: Uncompensated platform roll and pitch waviness. 52
Figure 3.2.4 B: 3-D LiDAR point cloud generation using raw GPS and IMU data. 53
Figure 3.2.4 C: Side view of bridge after using LiDAR-based altitude estimator. 53
Figure 3.2.4 D: Top view of bridge deck after using LiDAR altitude estimator. 54
Figure 3.2.4 E: 3-D LIDAR point cloud results after using scan-matching alignment. 54
Figure 3.2.4 F: GPS tracking over satellite image from Google Maps (red line). 55
Figure 3.2.4 G: Vision Marker 56
Figure 3.2.5.1 A: Tau 2 FLIR ® camera and ThermalCapture TeAx ® module. A Front of the camera showing the Tau 2 core, and B, ThermalCapture module being assembled and attached to the Tau 2 core. 57
Figure 3.2.5.2 A: A Concrete slab and simulated delaminations design (Design and drawing by K. Vanghefi) being made at Michigan Tech. B Styrofoam pieces locations in the slab molds before pouring the concrete, compare with the design in part A. 58
Figure 3.2.5.2 B: Comparison between FLIR SC 640 (left column) and Tau 2 (right column) cameras. Delamination Depths (DD) and image Acquisition Times (AT) (after turning off the IR lamp) are noted on each image. 60
Figure 3.2.5.2 C: Effects of noise reduction through image filtering. A Comparison between the noise levels of the Tau 2 and the SC 640 cameras. B through D, smoothing effects of applying low-pass filters (average and Gaussian) with different window sizes to an example delamination from the Tau 2 dataset. 61
Figure 3.2.6 A: Delamination mapping (delimited by green polygons) using different algorithms and threshold criteria. A through D correspond to a single threshold classification for the whole 8 bit (0 – 255 values range) image, thresholds being respectively 255, 240, 245, and 250 units. E was derived using a 100 x 100 pixel moving window and a threshold of 2 standard deviations above the mean. F was derived also with a 100 x 100 pixel moving window and a 90th percentile threshold. 64
Figure 3.2.6 B: ROC curves for the laboratory concrete slab experiments. Each row of graphs represents a different delamination depth: A, B, and C are 1 inch deep, D, E, and F are 1.5 inches deep, and G, H, and I are 2 inches deep. Each column of plots represent a different window size for the local threshold analysis: A, D, and G, resulted from a 50 x 50 pixel window, B, E, and H correspond to 100 x 100 pixel windows, and C, F, and I correspond to 150 x 150 pixel windows. The color codes of the curves correspond to the time in minutes for the acquisition of the thermal image, after powering off the heating lamp; color codes are the same for the three graphs on each row (therefore color codes are only given on the rightmost plot). Circles and triangles in each plot mark the 50th and 90th percentile threshold points, for which the parameters are also given in Table 3.2.6 A. Note how classifier performance degrades with deeper delaminations, smaller analysis windows, and longer times after heating (lower slab temperatures). 65
Figure 4.1 A: Seven mile stretch of Interstate-96, which was completely shut down for reconstruction. 67

Figure 4.1 B: Merriman East U-turn Bridge selected for a UAV assessment. 68
Figure 4.1 C: Stark Road Bridge selected for UAV assessment. 68
Figure 4.1.1 A: High-resolution image of Merriman Road East U-turn Bridge. 69
Figure 4.1.1 B: Full bridge length (left) high-resolution orthorectified image of Merriman East U-turn Bridge with zoomed-in northern (middle) and southern (right) sections. 70
Figure 4.1.1 C: Automatically detected spalls on the Merriman Road East U-turn Bridge. These totaled 150.0 square feet of the bridge deck, or 4.4 percent of the total deck area. 71
Figure 4.1.1 D: Full bridge length (left) hillshade image of Merriman East U-turn Bridge with zoomed-in northern (middle) and southern (right) sections. 72
Figure 4.1.1 E: High-resolution image of Stark Road Bridge. 73
Figure 4.1.1 F: Full bridge length (left) high-resolution orthorectified image of Stark Road Bridge with zoomed-in northern (middle) and southern (right) sections. 73
Figure 4.1.1 G: Full bridge length (left) hillshade image of Stark Road Bridge with zoomed-in northern (middle) and southern (right) sections. 74
Figure 4.1.1 H: Georeferenced thermal imagery acquired through the Tau2 and ThermalCapture camera system mounted on a UAV, overlaid on high resolution orthophotos, also acquired from the same UAV platform for Merriman East U-turn (left) and Stark Road (right). 76
Figure 4.1.1 I: Delamination areas that were confirmed in the field through hammer sounding tests. A View of the delamination locations (green dots) with their respective number labeled in white. B and C show a close-up view of delamination area 1, in the visible and thermal bands, respectively. Notice the absence of any noticeable signs of the delamination in the visible band (B), in contrast to the clearly visible area of higher temperature shown in the thermal band (C), and indicated by the blue circle. 77
Figure 4.1.1 J: GPS tracking (red line) superimposed on Google Maps satellite image. 77
Figure 4.1.1 K: 3-D LIDAR point cloud results of Merriman Rd. Bridge after using Michigan Tech LiDAR processing algorithm. 78
Figure 4.1.1 L: 3-D LiDAR point cloud of Merriman East U-turn bridge deck. 78
Figure 4.1.2 A: ROC curve parameters for the test site delamination points. Circles and triangles in each plot mark the 50th and 90th percentile threshold points, for which the parameters are also given in Table 4.1.2 A. Curve colors represent the different testing points, as annotated in the figure legend. Note that these ROC curves only compare the local percentile threshold with visual inspection methods, the latter being used as the “true” reference. 80
Figure 4.1.2 B: Distribution of pixel values for an eight bit multiband image of the bridge deck surface. Visible bans (red, green, and blue) are all grouped in a relatively narrow and coinciding band, corresponding to gray tones, while the thermal band values are extended over a broader and not very correlated range. 81
Figure 4.1.2 C: Combination of thermal (A) and visible (B) bands to control for false positives in the delamination classification and mapping process. Threshold classification of high temperature areas produces the map in C, but from inspecting the visible image (B) it becomes apparent that such areas show up as “hot” probably due to changes in the surface material. A map of pixels outside with values beyond 1.5 standard deviations from the local mean for the visible band is produced in D, and is used to control for the false positives: i. e. only pixels that show radiance values above the

local background and do not deviate much from the local mean in the visible band are classified as delamination pixels in E. This virtually eliminates all the pixels that originally were classified as delamination pixels based only on the thermal band threshod information. 84
Figure 4.1.2 D: Overview of the entire bridge-deck in the visible (A) and thermal (B) bands, with delamination areas shown by the blue polygons. A close-up view of a section of the deck is also presented in C (visible) and D (thermal), with delamination areas also shown by the blue polygons. 85
Figure 4.2 A: Overview of the Elm Street Pump Station along I-696 in Roseville, MI. 86
Figure 4.2 B: Overview of the River Rouge Pump Station in Southfield, MI. 86
Figure 4.2 C: The opening of at the Elm Street Pump Station that the micro UAVs flew through for the demonstrations. The I beam that caused an issue with the first attempt is on the lower left of the opening. The opening is approximately 4 feet x 3 feet. 87
Figure 4.2 D: The Walkera UAV having just lost control after making contact with the wall of the pump station. 87
Figure 4.2 E: The Heli-Max 1Si about to pass through the opening into the lower section of the pump station. 88
Figure 4.2 F: The Heli-Max 1Si right after passing through the opening into the lower section of the pump station. 88
Figure 4.2 G: An extracted frame from a micro UAV flight into the lower section of a pump station. 89
Figure 4.2 H: Looking up at the ladder and the opening of the River Rouge Pump Station from the lower level. 89
Figure 4.2 I: Heli-Max 1Si flying and collecting video of the River Rouge Pump Station. 90
Figure 4.2 J: The Walkera QR 100 flying in the River Rouge Pump Station. 90
Figure 4.2 K: Video being streamed back to a cell phone as the Walkera 100 is inspecting the River Rouge Pump Station. 91
Figure 4.3 A: The MTRI blimp at the ITS World Congress site on Belle Isle. 92
Figure 4.3 B. Screenshots from the MTRI blimp video feed of the emergency response mock incident. The blimp was approximately 100 feet in the air when these shots were captured. 92
Figure 4.4 A: The traffic monitoring blimp collecting near-live video data over Belle Isle during the ITS World Congress. 94
Figure 4.4 B: A screenshot of the near-live video feed that was shared through one of the Traffic Operations Center video walls. 95
Figure 4.4 C: Belle Isle Technology showcase attendees viewing a demonstration of the Bergen hexacopter UAV. 96
Figure 4.4 D: Project team member Michelle Wienert sharing the UAV project information with World Congress attendees. 97
Figure 4.4 E: A small DJI Phantom quadcopter (circled in yellow) being flown over the indoor ITS Test Track in the Cobo Exhibit Hall; onlookers are viewing the demonstration and the RCOC culvert piece can be seen on the lower right. 97
Figure 4.4 F: The traffic monitoring blimp video is being displayed in the top left of the MDOT ITS World Congress TOC south video wall, enabling attendees to see the type of near real-time traffic information that can be shared through this system. 99

Figure 4.4 G: A screenshot from the Youtube video that was used to help describe the MDOT UAV project to attendees during the Spotlight Presentation and at the Michigan Tech Technology Showcase booth. 100
Figure 4.4 H: PI Colin Brooks gave the Spotlight Presentation talk to ITS World Congress attendees. ... 100
Figure 4.4 I: The hexacopter UAV was able to take this photo of the Mock Incident and then share it immediately after completion of the flight. 102
Figure 4.4 J: The hexacopter starting to collect imagery during the Mock Incident. 102
Figure 4.4 K: An example of one of the images shared with Matt Brinker for display in the MDOT Aeronautics area; this one shows an overhead image of bridge deck patching and spalls collected with the hexacopter UAV. 103
Figure 4.4 L: A screenshot of the Michigan Tech News article released in advance of the ITS World Congress to help promote the project team's participation and MDOT's backing of advanced research. 104
Figure 5.1 A: Photos added to an AgiSoft project for processing. 106
Figure 5.1 B: A sparse point cloud produced from using the "Align Photos" command. 106
Figure 5.1 C: Setting the project coordinate system through the ground control panel. 107
Figure 5.1 D: A mesh has been generated over the point cloud to make a 3D model. 108
Figure 5.1 E: The Python Shell that is used to run the spall detection algorithm. 109
Figure 5.1 F: Differences in minimum spall sizes as generated from the spall detection algorithm. The first image one the left depicts all spall that are larger than 10 square centimeters (1.6 square inches), then 100 square centimeters (15.5 square inches), then 1000 square centimeters (155 square inches) All of the images are of the same location on Freer Road near Chelsea, MI. 110
Figure 6.2.1 A: A Kingfisher aerostat with sail that helps keep the aerostat from rotating in the wind and provides lift. The project's Samsung 4G camera or similar system could transmit near-real time video from this platform to a TOC. 120
Figure 6.2.3 A: Example crash scene image hexacopter-based collection demonstration from April, 2014 for SOCCIT. 122
Figure 6.2.3 B: SOCCIT meeting attendees viewing the UAV demonstration for crash scene reconstruction imagery. 122
Figure 6.2.3 C: Additional crash scene image collected by the hexacopter-based system at the ITS World Congress. 123
Figure 6.2.4 A: A) Location of Meyers site on M-10 highway northwest of downtown Detroit. B) Retaining wall section at Meyers site on M-10 highway. C) 3-D point cloud change detection showing movement in the wall panel starting at joint 4. 124
Figure 6.2.5 A: Overhead photo of a soil and gravel pile at a Michigan quarry that can be used to help estimate volumetric content of the pile and its change over time. 126
Figure 6.2.5 B: The I-96 Fix major MDOT road and bridge rehabilitation project in Livonia, MI as viewed during construction when the Interstate was closed to traffic. 126
Figure 6.2.5 C: Close-up photo of bridge bearings, a beam, and the top of a pier cap taken with a small DJI Phantom UAV that would have needed a bucket truck to take the equivalent image. 127

Figure 6.2.5 D: Example of automatically stitching together over 140 images taken with the hexacopter UAV to create a single 2.5 millimeter resolution orthophoto of a bridge deck with significant condition problems such as spalling. 128
Figure 6.2.6 A: A single 36 megapixel (resolution), 16 megabyte (file size) image taken of the Stark Road bridge deck. About 140 of these were needed to create the 3-D model of the bridge deck, all collected with three minutes of flight time. 130
Figure 6.2.7 A: Thermal images captured after 30 minutes of heating with the 336 x 254 sensor array camera, showing delaminations in concrete slabs at 1 and 2 inches depth. Blue colors are lower temperature while yellow to red colors correspond to increasing temperatures. The higher temperature corresponds to locations with known delamination. 131
Figure 6.2.7 B: Comparison of the Tau 336 x 254 and Tau 640 x 512 sensors based on ground pixel size and field of view. 132
Figure 6.2.8 A: Block diagram of high accuracy UAV-based simultaneous thermal/video/LIDAR measurement and fusion. 134
Figure 6.2.8 B: Three-dimensional scan of the MTU EERC and Dow buildings and surrounding areas. .. 135
Figure 9.3 A. Dispersion plot of paired pixel digital number and temperature[4] values, for one of the hot plate intercalibration experiments. A-47

List of Tables

Table 2.1 A: Comparison table displaying platforms with which sensors they carry and the MDOT job functions they can support, based on study results. 5
Table 3.2.6 A: ROC curve parameters for the laboratory concrete slab experiments. D is the delamination depth in inches. W is the analysis window width in pixels. T is the time in minutes of acquisition of the thermal image since the IR lamp was shot down (a proxy for cooling). AUC is the area under the ROC curve. FPR_{50}, TPR_{50} and $Accu_{50}$ are the false positive rate, true positive rate, and overall accuracy at a threshold of 50th percentile. FPR_{90}, TPR_{90} and $Accu_{90}$ are the false positive rate, true positive rate, and overall accuracy at a threshold of 90th percentile. 66
Table 4.1.2 A: ROC curve parameters for the test site delamination points. AUC is the area under the ROC curve. FPR50, TPR50 and Accu50 are the false positive rate, true positive rate, and overall accuracy at a threshold of 50th percentile. FPR90, TPR90 and Accu90 are the false positive rate, true positive rate, and overall accuracy at a threshold of 90th percentile. Note that these ROC curves only compare the local percentile threshold with visual inspection methods, the latter being used as the “true” reference. 79
Table 6.1 A: Implementation Action Plan checklist 117

1. Introduction

This report describes the accomplishments of the "Evaluating the Use of Unmanned Aerial Vehicles for Transportation Purposes" research project, contract number 2013-0067, project number Authorization No. 1, OR number OR13-008, as funded by the Michigan Department of Transportation (MDOT). Senior Research Scientist Colin Brooks of the Michigan Tech Research Institute (MTRI), a research center of Michigan Technological University ("Michigan Tech"), is the Principal Investigator of the project, with a period of performance of May 22, 2013 to November 30, 2014. Co-Investigators are Dr. Thomas Oommen of the Michigan Tech Department of Geological/Mining Engineering and Sciences and Dr. Tim Havens of the Michigan Tech Electrical and Computer Engineering Department.

1.1 Executive Summary

This report describes background information on each of the unmanned aerial vehicle (UAV) platforms, sensors, and types of infrastructure that have been included in the project. Five main UAV platforms were tested and demonstrated, including a Bergen hexacopter manufactured in Michigan (a six-bladed multi-rotor UAV, see Figure 1.1 A), a small DJI Phantom Vision 2 quadcopter, a smaller and more agile Blackout mini H quad UAV for confined space inspection, micro-UAV platforms, and a traffic monitoring blimp. The hexacopter (paired with optical and thermal sensors) was most appropriate for high-resolution imaging of transportation infrastructure, such as creating the automated calculation of the locations and volumes of spalls as well as locations of likely delaminations on bridge decks. The DJI Phantom quadcopter was shown to be useful for rapid imaging of a scene, such as a construction site. The Blackout mini H quad was capable of flying through and providing real-time video of the inside of a culvert. The micro-UAVs were able to send live video of the insides of two MDOT pump stations along I-696 near Roseville and Southfield – meaning that the safety of sending in a person into one of these confined spaces could be better evaluated. The traffic monitoring blimp demonstrated how near-live video (with only a 10-15 second delay) could be sent from the blimp using a relatively low cost 4G (cell phone network) capable camera.

Figure 1.1 A: A Bergen hexacopter, used in the project to collect optical, thermal, and LiDAR data for assessing bridge condition, roadway assets, and other transportation assets. Left – collecting bridge condition data; Right – close-up view.

Two bridges, two pump stations, two traffic sites, and a roadway asset site were all evaluated through UAV-based imaging through this project. Appropriate lab testing was also completed ahead of the field testing and demonstrations to ensure safe and efficient operations. The two bridges were sensed when a seven-mile stretch of I-96 was closed in Livonia, MI, which provided the ability to image bridges with poor condition decks during temporary closures. Undersides, substructure elements, and fascia were also imaged. From the optical camera (a Nikon D800 with 50 millimeter prime lens), a 2.5 millimeter merged image ("orthophoto") was created, along with a 3-D profile (a digital elevation model or DEM), and a GIS layer of spalls that were located and characterized using an automated spall detection algorithm. The project's thermal camera enabled detection of potential delaminations from a UAV platform. A light detection and ranging (LiDAR) sensor was used to create a three-dimensional (3-D) model of the bridge, and algorithms were developed to improve the positioning accuracy of LiDAR point cloud data. Optical imaging with appropriate algorithms was used for example roadway asset detection from UAV-based imaging. Pump station and culvert images and video were

shared with MDOT collaborators, and MDOT staff members attended both pump station demonstration sessions and were able to see the live video of the pump station interiors taken using the micro-UAVs.

Two new demonstration tasks were included in the project that were not part of the original objectives. One was crash scene reconstruction imaging, where two demonstrations were completed, one for a single Michigan State Police (MSP) officer, and another for a larger, almost 30-person group through the Southeast Oakland County Crash Investigation Team (SOCCIT). The potential for a larger, more formal demonstration effort exists, especially based on strong interest expressed by SOCCIT members such as the Bloomfield Township Police.

The second additional effort was to present MDOT UAV research capabilities through participation in the 21st World Congress on Intelligent Transportation Systems (ITS) held in Detroit on September 7th to 11th, 2014 at Cobo Hall and Belle Isle (this event is also known as the ITS World Congress). In the end, the project team participated in the ITS World Congress in ten different ways (see Section 4.4), ranging from UAV demonstrations at Belle, near-live traffic monitoring blimp imagery being sent to one of the two MDOT Traffic Operations Center video walls inside Cobo Hall, giving Spotlight and Technical session presentations, and participating in the Emergency Responder Day Mock Incident with UAV demonstrations and imagery sharing. MDOT was able to add initiatives for these in-depth demonstrations at the ITS World Congress, and provide exposure to MDOT in backing advanced technological research that is useful to the ITS community.

Through these extensive testing, field demonstration, and outreach efforts, UAV technologies have been shown to be useful for transportation purposes. Bridge deck assessment, traffic monitoring, roadway asset detection, improved LiDAR and thermal data processing, and confined space inspection have all been advanced towards practical usage and implementation. An Implementation Action Plan (IAP) is included as Section 6 of this report, including the normal IAP sub-sections, plus a series of eight recommendations for future research. These include 1) operations (traffic monitoring) and maintenance uses and demonstration costs savings as a result of UAV technology, 2) Providing data to the MDOT Data Use Analysis and Process project, 3) more formal crash scene imaging, 4) slope stability assessment, 5) aerial imaging to meet MDOT Survey Support and related needs, 6) optimal methods to store and share large UAV-based data sets, 7) improvements to UAV-based thermal imaging, and 8) multi-sensor high-accuracy UAV positioning,. These ideas could be modified or added to depending on MDOT priorities and available funding. The project team looks forward to the opportunity to continue helping MDOT take advantage of the increasing capabilities of rapidly advancing UAV technology.

1.2 Hypothesis, Objectives, and Scope

The final work plan for this project stated that advancements in remote sensing technology using an UAV would provide "the opportunity to take this technology to the next level by providing ready, rapidly deployable access in locations that are potentially challenging to inspect at higher resolutions than current methods are capable of." The main hypothesis was that these remote sensing techniques can provide objective non-destructive testing of critical components of transportation infrastructure. The objectives and resulting scope of the study were defined in the work plan as:

- Develop, test, and demonstrate how UAV technology can help provide visual inspections from above for a variety of structures and locations of interest to MDOT, such as pump stations, roadway assets, and entrances to sewers and culverts.
- Provide a demonstration of how a rapidly deployable, relatively inexpensive UAV system could be deployed to monitor traffic over an extended period without the need for new permanent infrastructure.
- Investigate non-destructive evaluation techniques using remote sensors on a UAV platform to evaluate the surface and structural integrity of bridge elements, including using thermal infrared and 3-D optical non-destructive evaluation (NDE) methods.
- Demonstrate how a LiDAR sensor could be used to rapidly assess and inspect transportation infrastructure.
- Provide a review of the current state-of-the-practice with a focus on practical UAV deployments by other transportation agencies including through up-to-date academic research projects.
- Provide recommendations and an implementation plan on utilizing the UAV technology for MDOT infrastructure inspections and asset management data collection.

All of the above objectives have been met through execution of the project over its current duration, and have led to potential additional deliverable tasks that build from the project's demonstrations, data, and analyses; these logical recommendations for future research were mentioned above are described in Section 6.2 below.

1.3 State of the Practice for Remote Sensing of Transportation Infrastructure Using Unmanned Aerial Vehicles (UAV)

Also included as part of the project was a State of the Practice Report that included an extensive literature review; this is included as the second appendix in this report (section 9.2). It reviews non-destructive evaluation (NDE) remote sensing techniques, different platforms, example applications, and current uses of UAVs for transportation infrastructure assessment. An included literature review has five pages of references, 79 in all, covering a wide variety of UAV applications and sensing methods.

The State of the Practice report served the project team as a useful summary of UAV capabilities and representative systems as of late 2013, and helped inform MDOT on what methods, systems, and application could be addressed through the use of UAVs. Examples of recent UAV testing and deployments by the Washington State Department of Transportation, the Florida Department of Transportation, the Hawaii DOT, Ohio DOT, and the New Jersey DOT were included. It was clear to the project's report authors that there was a strong potential to apply UAVs to meet transportation infrastructure assessment needs.

2. UAV Platforms – Technology Overview

2.1 Aerial Equipment

The following sections describe the various aerial platforms used to accomplish the project research tasks and are included to give a detailed overview of their characteristics. The following table (2.1 A) provides a summary of these details, organized by platform (rows) and sensors (columns), with a description of the MDOT job function they can support, based on this project's study results.

Table 2.1 A: Comparison table displaying platforms with which sensors they carry and the MDOT job functions they can support, based on study results.

Platform / Sensor	Nikon D800 camera	Hokuyo UTM-30LX-EW LiDAR	Tau 2 FLIR thermal camera	Integrated Camera	GoPro camera	Samsung 4G Camera
Bergen Hexacopter	Bridge Deck Inspection through 3D modeling	Roadway assets	Delamination detection			
DJI Phantom Vision 2				Bridge stucture imaging, construction site monitoring		
Blackout Mini H Quadcopter				Bridge stucture imaging, Confined space assessment, Culvert Inspection		
Heli-Max 1 Si				Confined space assessment		
Walkera QR 100S				Confined space assessment		
FPVfactory Mariner Waterproof Quadcopter					Bridge stucture imaging - undersides (*For bridges over water*)	
Blimp						Traffic monitoring / operations and maintenance

2.1.1 Multi-rotor Helicopters

2.1.1.1 Bergen Hexacopter

The Bergen Hexacopter is a multi-rotor helicopter that is produced by the Bergen R/C (remote control) Helicopters which is based near Cassopolis, MI (approximately 40 miles southwest of Kalamazoo, MI). These UAVs are designed to carry a camera payload for capturing pictures or video (Figure 2.1.1.1 A). A wide variety of payloads can be mounted with the max payload capacity being 11 pounds with a flight time of up to 18 minutes under standard operations, with the potential to fly up to 30 minutes. A typical cost for the hexacopter, without sensors, is $5400 including a set of spare batteries.

Figure 2.1.1.1 A: Bergen Hexacopter

There is a global positioning system (GPS) receiver on the hexacopter which enables it to hold its position while in "GPS" mode. While in this mode, if the pilot were to stop providing input into the controller and the throttle was at 50 percent, the hexacopter would maintain its altitude and position. This system is able to compensate for wind and generally holds the UAV within a 1 meter box. If the hexacopter was switched into "Attitude" mode, the flight control with only keep it stable and level and it will not use the GPS to hold its position. An added advantage of flying while in GPS mode is a return to home feature. If the hexacopter loses connection to the controller it will ascend to 150 feet, fly back to its "home" position and land itself. The home position is set when the hexacopter is turned on and GPS locks onto satellites. The DJI controller can also be set to initiate the return to home function if the battery voltage drops down to a specified level or by toggling a predefined switch on the controller.

The six rotors provide an advantage over single rotor helicopter based systems. When compared to hexacopters, single rotor helicopters are less stable, produce more vibration, and are more difficult to fly. There is also the added benefit that hexacopters are also easier to

maintain. Single rotor helicopters have over 50 connectors and moving parts that control the main and tail rotors. These all have to be checked before each flight to prevent loss of control. By comparison, a hexacopter only has 10 moving parts. Six are the motors themselves and the other four are the folding arms (these folding arms make the device very easy to transport, including inside the back of small cars). The operator only needs to make sure the wires are not loose and tighten the folding arms in place, making this type of multi-rotor device safer that single rotor remote control helicopters.

The camera is mounted on a two-axis gimbal under the body (Figure 2.1.1.1 B). While in flight, the gimbal is able to compensate for roll and pitch movements of the hexacopter. This keeps the camera pointed in the same direction at all times independent of the hexacopter's movements. The gimbal is also able to change the viewing angle of the camera using a switch on the remote control. This switch allows the pilot to point the camera at any angle from straight forward to down.

Figure 2.1.1.1 B: Close up of a Nikon D800 mounted to the gimbal under the hexacopter.

Underneath the gimbal is a smaller camera that is used as a first person viewer (FPV) (as shown in Figure 2.1.1.1 B). This camera has roughly the same field of view (FOV) as the Nikon D800 with a 50 millimeter prime lens. This allows the operator to see exactly what the camera is imaging during flight. The high definition (HD) video from the camera is transmitted to a hand held monitor. This monitor also displays other important information about the flight, including battery voltage, altitude and speed.

2.1.1.2 DJI Phantom Vision 2

The DJI Phantom Vision 2 is a small quadcopter (http://www.dji.com/product/phantom-2-vision), available on Amazon for $799 (as of Oct. 21, 2014) that comes with an integrated 14 megapixel (mp) camera, onboard GPS, rechargeable battery capable of 25 minutes of flight time, and real-time video capabilities via a Wi-Fi range extender and smart phone app. The 14

megapixel camera sensor is capable of taking both JPEG and RAW image formats, can record 1080p HD video, and its wide angle lens photos can be corrected to a more “normal” look using an Adobe lens profile. The camera sensor and lens quality and type are not designed for making measurements or other uses needed high-resolution, high-quality imagery, but are meant for rapid, easy-to-collect aerial photography.

Figure 2.1.1.2 A shows the small device, 14.6 inch width x 8.3 inch height x 13.2 inch depth in size and 2.6 pouds (1.1 kilogram) in weight. It has a reputation for being easy to learn to fly (and easy to fly) and having a wide user community. With the ability to take still images and record video (to microSD cards) with a real-time video link of up to 300 meters (up to about 900 feet), it is very useful for applications where quick aerial images are needed. Federal Aviation Administration (FAA) guidelines mean that it should not be flown above 400 feet; in practical testing, heights of up to 250 feet provided useful aerial imagery that would normally have required a helicopter or very low flying airplane to collect. It can fly in relatively challenging areas, such as underneath bridges and inside some confined spaces. It includes a safety ability to “fly to home” if loss of communication with the controller occurs, and a software update now enables it to fly to pre-set waypoints. An older DJI Phantom 1 was also used to directly image the underside of bridges, as it could mount a small (GoPro) camera on top to shoot photos straight up.

Figure 2.1.1.2 A: The DJI Phantom Vision 2 small quadcopter UAV

Example results are included in the lab testing and field demonstration / results sections below. For this project, uses included taking photo inventories of study sites, bridges (of the deck surface, deck underside, and hard to reach areas such as pier caps, beam sides, and bearings), a pump station interior, a construction site (see Figure 2.1.1.2 B), a crash scene reconstruction demonstration, the inside of Cobo Hall, and the ITS World Congress Belle Isle demonstration area. If MDOT needs to ability to quickly see an area from above, then this easy-to-operate and

relatively inexpensive UAV tool can be a helpful part of its data collection capabilities, and could be an early implementation example.

Figure 2.1.1.2 B: An example DJI Phantom 2 collected JPEG image with lens correction, of part of the closed stretch of I-96 in Livonia, MI. These types of quick aerial photos can be useful for construction site monitoring and imaging transportation assets and traffic conditions.

2.1.1.3 Blackout Mini H Quadcopter

The Blackout Mini H Quadcopter is a small quadcopter frame (http://www.minihquad.com/), available in kit from the Blackout Mini H Quadcopter website for $382 almost ready to fly (ARF). This aerial vehicle is designed to be highly agile and customizable, making it an ideal base platform on which to develop a system for deployment in confined spaces. An Ardupilot Mega open source flight controller ($50) was paired with a 3-D Robotics uBlox GPS/Compass module for control of the system. This Arduino-based flight controller provides the option to add application specific sensors to the platform in the future for flight control, e.g. a rangefinder(s) for automatic positioning in a confined space. The MTRI Blackout is also equipped with a FatShark FPV 720p system which enables the user to see what the Blackout "sees" and permits flying without being able to see the aircraft, which is useful in confined spaces. The camera module of this system also records the video stream to a standard microSD memory card. This system is available from Amazon for $430 (as of Oct. 24, 2014). This system can be used with any four channel (or greater) radio system.

Figure 2.1.1.3 A shows the assembled MTRI Blackout Mini H Quadcopter. This system has dimensions of 11 inch x 13 inch x 3 inch and has a mass of 1.50 pounds. This platform is more difficult to fly than other platforms due to its custom nature and the ability to have control over the software in the flight controller. As such, this platform should not be flown by a novice user, but instead one who has experience flying other UAVs such as a DJI Phantom. Part of the

reason for this is the MTRI platform is intended to fly in confined spaces, and therefore will not be able to rely on the GPS or compass sensors for stabilization purposes. Flying the platform without these sensors requires more skill from the user. The open source design of the flight controller will allow appropriate sensors to be added to the platform in the future to assist in stabilizing the platform in these confined spaces.

Figure 2.1.1.3 A: MTRI Blackout Mini H Quad

Presently the testing of this platform has been focused on flying it inside a section of used culvert (see Figure 2.1.1.3 B) shared by the Road Commission for Oakland County. Further testing inside other confined spaces and sensor integration are needed before this platform is a fully deployable system. Flight time is estimated at 10-15 minutes in the current configuration.

Figure 2.1.1.3 B: Blackout Mini H Quad flying inside a culvert.

2.1.1.4 Waterproof Quadcopter

The FPVfactory Mariner Waterproof Quadcopter (http://www.fpvfactory.com/products/mariner-accessory/mariner-rtf/fpvfactory-waterproof-quadcopter-mariner-rtf-kit-fly-with-gopro-waterproof-camera-625.html), is available on

Amazon as a ready to fly (RTF) package for $918. This includes the same flight control system found in a DJI Phantom, a Naza Lite controller, for flight stabilization and GPS positioning. This platform has then been paired with a GoPro Hero 3 camera ($330) and its suction cup mount ($40). This permits the gathering of 1080p HD video at 48 frames per second, or 12 megapixel images at 2 frames per second. The camera can be mounted on either the bottom or the top of the aircraft and can be pointed to any angle. It is also possible to carry two cameras, both top and bottom mounted, at the same time. Flight time with a single camera is estimated at 15 minutes.

Figure 2.1.1.4 A shows the Mariner, having dimensions of 24 inch x 24 inch x 8 inch and a mass of 4 pounds. This system is essentially the same system as a DJI Phantom, however it is completely waterproof. This system is suited to flying underneath bridges built over water or floating on the water surface and “boating” underneath the bridge. This platform as versatile in its potential uses as a DJI Phantom and has the same flight control options, but the added waterproof nature eliminate the cost of “accidents” that could occur when collecting imagery while over wet environments.

Figure 2.1.1.4 B shows an image extracted from 1080p HD video taken using the Mariner with a GoPro camera. This image is the underside of a pedestrian bridge located over water on Belle Isle, Detroit, MI. The platform took off and landed on the water on either side of the bridge.

Figure 2.1.1.4 A: FPVfactory Mariner Waterproof Quad

Figure 2.1.1.4 B: Underside of a Belle Isle Bridge taken using the Mariner Waterproof Quadcopter

2.1.1.5 Other Micro-UAVs

Micro UAVs such as the Walkera QR 100S and Heli-Max 1 Si are quadcopters that are small enough to fit in the palm of a hand. These small UAVs are useful for confined spaces as they could easily fly through doorways, through rooms, and inside culverts. An onboard gyroscope helps to stabilize the quadcopters in flight but they do not have onboard GPS like the larger UAVs. These two UAVs are also very inexpensive when compared to the other multi-rotor helicopters with a price of less than $200 each.

The Heli-Max 1 Si has a flight time of 10 minutes and it has a small camera that is able to capture 720p video or 1 megapixel stills (Figure 2.1.1.5 A). A micro SD memory card of up to 32 gigabytes can be used to save video from the camera. The Heli-Max is 5.44 inches x 5.44 inches and is 1.77 inches tall with a weight of 0.10 pounds (46 grams).

Figure 2.1.1.5 A: Heli-Max 1 Si micro-UAV

The Walkera QR 100S is similar to the Heli-Max in size (5.7 inches x 5.7 inches) with a weight of 0.20 pounds (89 grams) (Figure 2.1.1.5 B). The flight time is also 10 minutes and it has an onboard camera. An advantage of the Walkera is that the camera can transmit the video live to a smart phone or tablet. Video and stills are saved to the external device (smart phone) as there is no onboard storage capacity.

Figure 2.1.1.5 B: Walkera QR 100S

2.1.2 Blimp

A blimp or aerostat is a different kind of unmanned aircraft than the rotary wing or fixed wing aircraft reviewed so far. Blimps/aerostats consist of an envelope made of a gas-impermeable material that is either a spheroid in the case of an aerostat or a teardrop shape in the case of what generally is considered a blimp. Stabilizing fins are generally added to the back of the envelope to help keep a blimp pointed into the wind. Aerostats often have an added airfoil or stabilizing fabric wing that keeps the aerostat stable and minimizes altitude loss as winds increase. Figures 2.1.2 A and 2.1.2 B show examples of small blimps/aerostats capable of deploying the types of digital cameras described earlier in this report that could be used for traffic monitoring. Figure 2.1.2 A below is a small blimp used by MTRI as a proof of concept for a traffic monitoring aerostat. The blimp is ~15 feet long and 5.5 feet in diameter; it requires about 300 square feet (8.5 square meters) of helium (just about one tank of helium) to fill. Net lift is ~8 pounds (3.6 kilograms); working lift is approximately 50 percent of net lift or 4 pounds (1.8 kilograms). The blimp can be safely flown in winds up to 15 miles per hour.

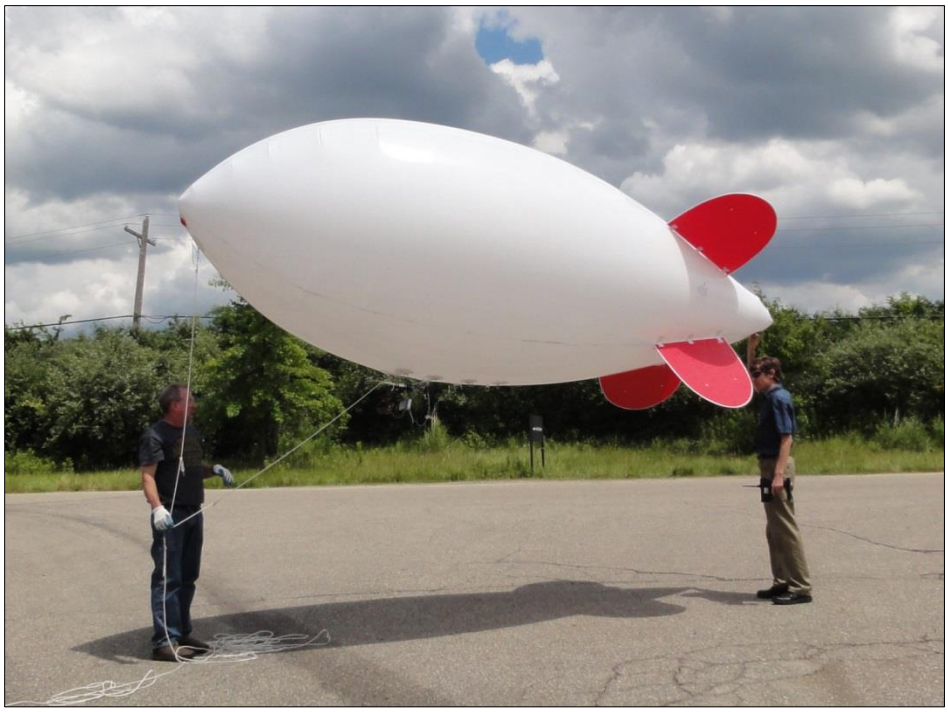

Figure 2.1.2 A: The MTRI blimp being readied for a test flight. Note the camera mounted on a 3 axis gimbal under the blimp.

Figure 2.1.2 B: A 35 meters cubed Allsopp Helikite in flight. This image illustrates the airfoil and keel that stabilize and provide some lift to the aerostat.

Aerostats/blimps are useful for applications that require temporary but persistent observation of an area on the ground. Aerostats can provide a traffic monitoring option that can remain on station for several days at a time, much longer than fixed or rotary wing battery or fueled-

powered UAV systems. Aerostats allow easy changing of view/perspective/altitude of the camera based on monitoring requirements. An appropriately sized aerostat also allows for a variety of sensor packages to be flown.

MTRI evaluated small blimps and aerostat systems from several vendors. Many aerostat options are available at different price points. Our September and October 2013 review of various aerostat vendor options completed for the State of the Practice report found most commercial aerostat systems are too large for our purposes or are targeted at the larger military/homeland security market and are priced accordingly (i.e., very expensive). Several vendors have offerings that appear to be aimed at the civilian aerial photography market – commercial property and high end residential photography appear be the target market for these systems. These or similar aerial photography systems are a better initial fit for traffic monitoring than the larger aerostats. MTRI selected a small advertising blimp for our demonstration project based on its ability to lift the load that was proposed (about 4 pounds) with enough of a buffer to allow for variations in wind speed and load (Figure 2.1.2 C). The load to be flown is a 3 axis gimbal and a 4G camera that transmits video for display in near real time via a web browser (Figure 2.1.2 D). This stream can be accessed using any device that supports a web browser from a desktop PC to tablets and smart phones (Figure 2.1.2 E).

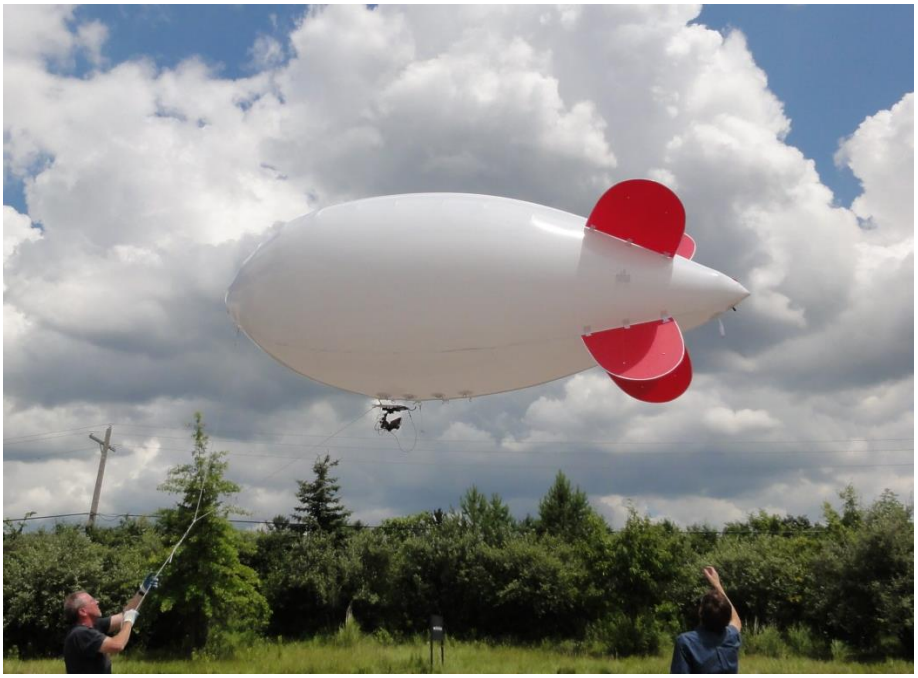

Figure 2.1.2 C: The MTRI blimp being launched for a test flight. The gimbal and camera are visible under the blimp.

Figure 2.1.2 D: The gimbal and camera assembly under the blimp. The battery on top of the gimbal supplies power to the gimbal.

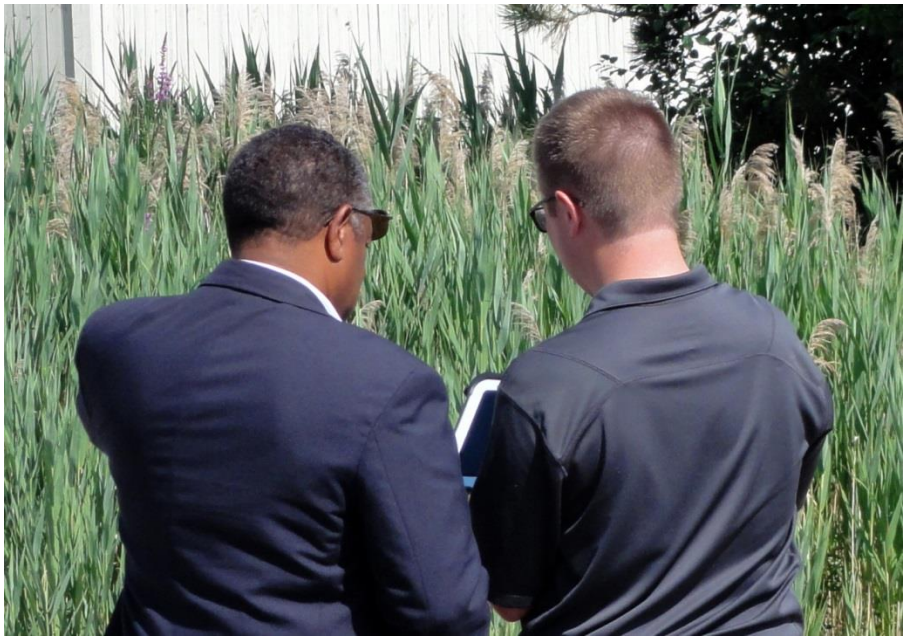

Figure 2.1.2 E: Ben Hart from MTRI (R) and Andre Clover (L)from MDOT viewing the video feed from the blimp camera on a rugged tablet during testing at MTRI.

Weather is a concern for all types of aircraft; rain and wind are particular concerns for aerostats as rain can reduce the available lift and strong wind can force the aerostat/blimp down and out

of position. Wind becomes a concern for small blimps at or around 15 miles per hour; different aerostat designs can handle much stronger winds.

Payload size is a variable that is generally handled by changing the size of the blimp/aerostat. Generally, the operating payload (everything that is going to be lifted, including the tether) should equal approximately 50 percent of the net lift of the aircraft. Operation in cool dense air increases the available lift while hot humid air tends to decrease lift.

The FAA's operating requirements for an aerostat are much less restrictive than those for other UAVs. Generally, operations below 150 feet do not require FAA notification although it is good practice to notify the FAA so a notice to airmen (NOTAM) can be issued if the aerostat will be on station for an extended period of time. Aerostats cannot be operated within five miles of an airport unless a waiver is issued by the FAA and if operated above 150 feet the tether must be marked by flags every 50 feet. The aerostat must be more than 500 feet from the base of any cloud.

2.2 Sensors

The following sections describe the various sensors and technology behind those sensors that were deployed from UAVs that used to accomplish the project research tasks and are included to give a detailed overview of their characteristics and capabilities.

2.2.1 Optical / Photogrammetry

Optical remote sensing is most commonly done by using sensors that are sensitive to the visible portion of the electromagnetic spectrum. This corresponds to wavelengths of light are between 400 and 700 nanometers. Optical systems are able to detect near infrared (IR) wavelengths of light (approximately 700 to 1300 nanometers or 1.3 microns) but use filters to prevent them from being detected by the sensor; however, digital cameras can have their filter removed. The most common optical sensors are charge-coupled devices (CCDs), which are used in typical consumer-grade digital cameras. The wide scale availability of digital cameras and low cost make them a good candidate for remote sensing applications. These sensors have been developed to be smaller as they are used for cell phone cameras as well as in professional photography.

Optical-based UAVs have been successfully used to measure 3-D point clouds, e.g., in archeological surveys (Barazzetti et al., 2010, Chiabrando et al., 2011), vegetation monitoring (Sugiura et al., 2005, Laliberte et al., 2011, Hunt et al., 2010), and forest monitoring (Tao et al., 2011, Dandois and Ellis, 2010).

For application on UAV platforms, there needs to be a balance between size of the sensor (i.e. weight) and resolution. High resolution digital single-lens reflex (DSLRs) cameras are able to capture imagery at over 20 megapixels but that comes at the cost of weight. The Nikon D800

cost less than $3,000 but it currently offers one of the highest resolution sensors on the market. The sensor is 36.3 megapixels which is capable of producing high resolution (< 0.3 inch pixel size) imagery while being flown at a distance of 100 feet from the target (Brooks et al. 2013) using a 50 millimeter prime lens. A GPS is also attached to the camera allowing for geotagged imagery. The disadvantage of this camera on a UAV platform is the size and weight. This camera can only be carried by the project's Bergen Hexacopter as the camera and lens weigh about 2.5 pounds (Figure 2.2.1 A). These types of cameras are more suited to be used for capturing imagery of bridges and other road infrastructure that may need high-resolution assessment of their condition, such as detecting and characterizing spalls (potholes).

Figure 2.2.1 A: Example of a Nikon D800 mounted below a Bergen Tazer 800 single rotor UAV ready for deployment.

Some UAVs such as the DJI Phantom Vision 2 have a built in camera that could be used for inspection purposes. Further detail of the Vision 2 is discussed in Section 2.1.1.2 and also http://www.dji.com/product/phantom-2-vision/spec. Other smaller UAVs have built in cameras for that can be used for the inspection of confined spaces. These smaller cameras such as those found in cell phones are the smallest cameras that can be practically used in micro-UAVs. Figure 2.2.1 B shows a Crazyflie Nano quadcopter (3.5 inches across) with a keychain camera mounted to it. The camera is capable of taking 2 megapixel HD video. Some micro-UAVs like the Heli-Max 1 Si and the Walkera QR 100S have these types of cameras already built in.

Figure 2.2.1 B: Crazyflie Nano (3.5 inches across and weighs 19 grams) with a keychain camera mounted on top.

Aside from acquiring photo inventories or transmitting video of bridges, confined spaces, and other transportation infrastructure, the photos taken from a UAV can also be used to extract additional, three-dimensional information through photogrammetric techniques. Photogrammetry is "the science or art of deducing the physical dimensions of objects from measurements on photographs of the objects" (Henriksen 1994). This includes measurements made from both film and digital photography. Digital photogrammetry has been demonstrated as a viable technique for generating 3-D models of structures and structural elements (Maas and Hampel 2006). In order to perform 3-D photogrammetry, the photos need to be taken with at least a 60 percent overlap (McGlone et al. 2004). This ensures that a feature on the ground is represented in at least two photos, as illustrated in Figure 2.2.1 C. At the altitudes that most UAVs will operate this technique is more specifically called close-range photogrammetry. Close-range photogrammetry is defined as capturing imagery of an object or the ground from a range of less than 100 meters (328 feet) (Jiang et al. 2008).

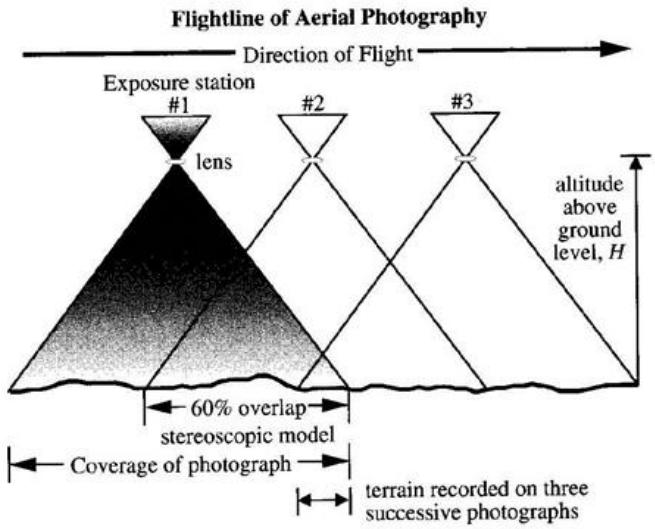

Figure 2.2.1 C: An example of how stereoscopic imagery for generating 3-D models is collected (Jenson 2007).

Typically, 3-D models are generated by using the bundle adjustment principle (Triggs et al. 2000). This process used determines the orientation of each image in a series of overlapping images to generate a sparse point cloud (Triggs et al 2000). Figure 2.2.1 D shows the triangulation between multiple images that is used during this process. This process allows for images to be taken at different angles, which occurs when the camera rolls and changes pitch as it is moved across its target.

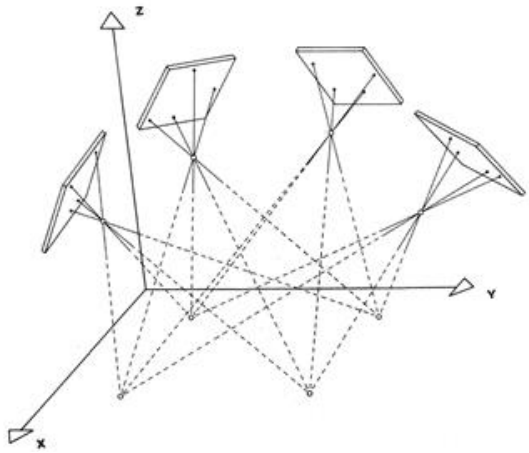

Figure 2.2.1 D: Bundle adjustment seeks to solve the geometry between photos and to generate 3-D point clouds. This figure shows the relationship between four images that is solved by the bundle adjustment (Wester - Ebbinghaus 1988).

This technique allows for additional height information to be extracted from the imagery. Various distresses, such as spalls, cracking, and ruts can be detected and characterized by generating digital elevation models (DEMs) from this additional three-dimensional data. With recent advances in close range photogrammetric software, the generation of DEMs is mostly automated. Some software applications, such as Agisoft PhotoScan, only require the user to input the photos and a 3-D model is generated without any further interaction. In order to generate a DEM the user has to set up a real-world projected coordinate system. This is done by placing markers with known GPS coordinates on the surface being modeled or by geo-tagging the images as they are taken. This technique was used by Ahlborn et al. (2013) to locate spalls on bridge decks with a truck-mounted camera and also by Brooks et al. (2013) to characterize distresses on an unpaved road.

2.2.2 Thermal

The basic concepts of thermal remote sensing presented in this section follow the general description given in standard text book on remote sensing (e.g. Jensen, 2007); for a more detailed explanation of these concepts the reader should consult such a text and the references therein. Section 3.2.5.1 describes the actual thermal imaging device used to collect bridge condition-related data. Thermal remote sensing is based on the physical process by which physical surfaces radiate electromagnetic energy as a function of their temperature. The thermal remote sensing instruments usually sense and record the radiance reaching the sensor after being emitted by the hot surface located at some distance from the instrument. The intensity and spectral content of the radiated energy depends not only on the surface temperature, but also on the material properties, especially the emissivity. The relationship between surface temperature and emitted electromagnetic energy can be described based on the concept of an ideal surface, known as a blackbody radiator, which absorbs all the incident radiation (the is no energy reflected) and only emits energy as a function of its temperature, according to Planck's law (see Equation 2.2.2 A), as shown in Figure 2.2 A.

$$B_{\lambda}(T) = \frac{2hc^2}{\lambda^5\left(e^{\frac{hc}{\lambda k_B T}}-1\right)} \qquad \text{Equation 2.2.2 A.}$$

Where B_{λ} is the spectral radiance given in Watts per square meter per steradian (solid angle unit) per micrometer (W m^{-2} sr^{-1} μm^{-1}); *h* is the Planck constant (6.62 x 10^{-34} Joule seconds); *c* is the speed of light in meters per second; $\boldsymbol{\lambda}$ is the wavelength of the radiation in meter; k_B is the Boltzmann constant (1.38 x 10^{-23} Joules per $Kelvin^{-1}$); and T is the temperature in Kelvin.

Real objects (sometimes called "gray bodies") do not behave as ideal blackbody radiators and emit less electromagnetic energy than would be emitted by a blackbody at the same temperature; the ratio of energy emitted by a real surface to that emitted by an ideal

blackbody radiator at the same temperature is called the emissivity, it is always a value between 0 and 1 (1 being the emissivity of a blackbody radiator), and is a property of each specific surface.

In the case of remote sensing systems, the electromagnetic energy emitted by a surface travels through the atmosphere before reaching the sensor. As the electromagnetic radiation travels to the atmosphere part of it is absorbed and scattered, but the rest is transmitted and reaches the sensor. The atmospheric absorption and scattering of electromagnetic radiation depends on the gases and particles in suspension present in the atmosphere, and on the wavelengths of the electromagnetic radiation. A "clear atmosphere" commonly absorbs mostly in well-defined regions of the spectrum as shown in Figure 2.2.2A. From this figure it can be seen that some regions of the spectrum allow radiations to be transmitted without much absorption, and such "atmospheric windows" are then exploited for remote sensing purposes. Additionally, the atmosphere also emits electromagnetic energy in the thermal part of the spectrum, which has to be taken into consideration as well.

By integrating the spectral radiance given by Planck's law over the entire range of wavelengths and directions (solid angles) we can derive another useful relationship, the Stefan-Boltzmann law, which relates the emissive power (amount of energy radiated per unit area and unit time) to the blackbody temperature (Equation 2.2.2 B):

$$j = \sigma T4 \qquad \text{Equation 2.2.2 B.}$$

Where *j* is the emissive power in Watts per square meter (W m^{-2}); σ is the Stefan-Boltzmann constant (5.67 x 10^{-8} watts per square meter per Kelvin (W m^{-2} K^{-4}); and T is the temperature in Kelvin.

This law applies only to ideal blackbody radiators (emissivity = 1), and for a real object with an emissivity of less than 1 the actual emissive power will be less by a factor given by the emissivity. From this it follows that the real temperature will also depend on the emissivity according to Equation 2.2.2 C.

$$\varepsilon = \left(\frac{T_{\text{brightness}}}{T_{\text{kinetic}}}\right)^4 \qquad \text{Equation 2.2.2 C.}$$

Where ε is the emissivity (non-dimensional), $T_{brightness}$ is the temperature that would correspond to a blackbody surface emitting the observed radiance, and $T_{kinetic}$ is the real temperature of the surface.

For this reason the emissivity of the surface becomes crucial in relating the temperature we want to measure to the radiance recorded by the remote sensing instrument. Emissivity values for opaque, dark colored materials tends to be high, close to 1 (e.g. > 0.9 for asphalt and rough

concrete), whereas emissivity values for highly reflective surfaces can be very low, close to 0 (e.g. < 0.1 for polished metallic surfaces).

Summarizing the theoretical overview, it can be said that the sensors used in thermal remote sensing usually sense and record the radiance reaching the sensor, and therefore additional data processing is necessary to derive more commonly used physical quantities, like temperature or emissive power. The main variables to consider are related to the atmospheric absorption and the properties of the emitting surface, in particular its emissivity.

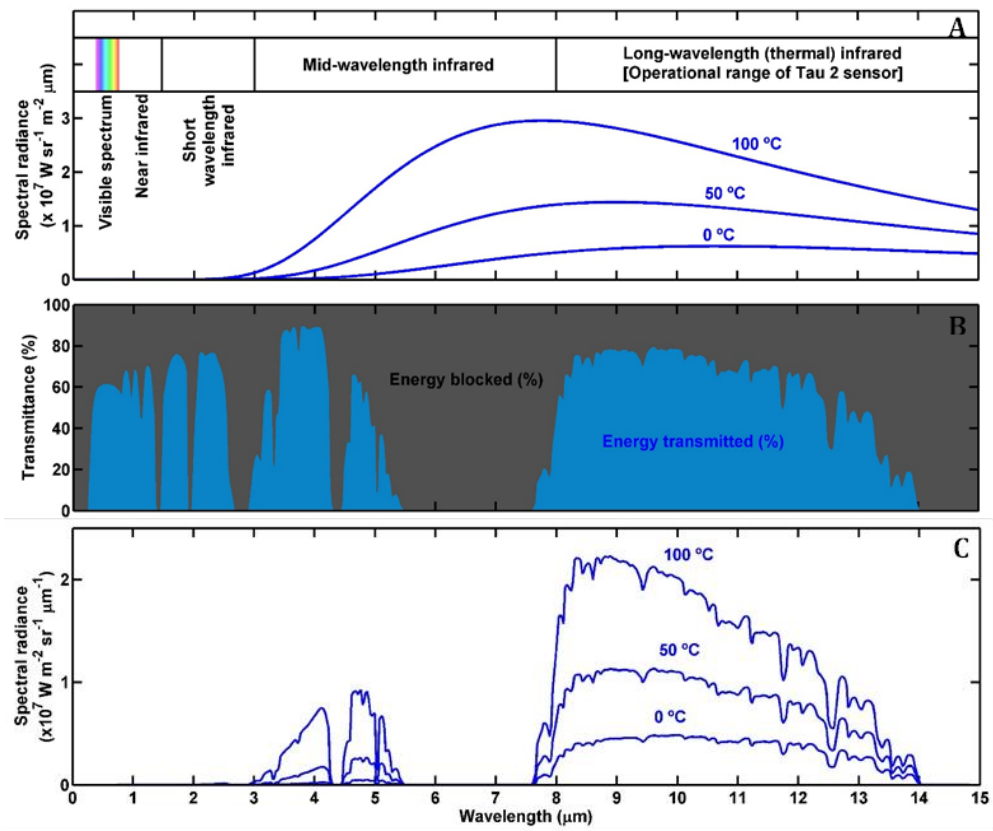

Figure 2.2.2 A: A - Spectral radiance as a function of wavelength according to Planck's law. The three curves represent surfaces at different temperatures. The upper extreme of part A also shows the classification of different regions of the electromagnetic spectrum, including the long-wavelength or thermal infrared region, on which most thermal remote sensing instruments work, including the forward looking infrared (FLIR) Tau 2 sensor discussed later. B -Typical atmospheric transmittance through a whole vertical atmospheric column (adapted from Loubere, 2012) for the same wavelengths shown in panel A. Notice the "thermal window" between 8 and 14 micrometers coinciding with the thermal infrared part of the spectrum, and for which the atmospheric transmittance is high, allowing electromagnetic radiation to travel without much absorption. C - Spectral radiance transmitted through the atmosphere considering the transmittance shown in panel B.

2.2.3 LiDAR

Small UAVs (using the FAA definition of all ones under 55 pounds) have attracted significant interest for a wide range of applications, from surveillance (Croom et al., 2004, Kim et al.,

2003), search and rescue (Bourgault and Durrant-Whyte, 2004), culvert inspection (Serrano, 2011), 3-D mapping (Jutzi et al., 2013), atmospheric measurement (Rogers, 2013), and forest inventory (Wallace et al., 2012).

For infrastructure inspection and, more specifically, transportation infrastructure, there has been some research into using small UAVs. Lin and Saripalli (2012) developed a method to detect and track roads from imagery taken from a micro-UAV. Serrano (2011) developed a quadcopter platform for inspecting culverts. Jiang et al. (2013) developed a UAV-based system for power line inspection. Russ et al. (2012) developed a system for detecting car-like objects in an earth-fixed point cloud measured via LIDAR on a small UAV.

Vision-based systems have been successfully used to create and measure 3-D point clouds including in archeological surveys (Barazzetti et al., 2010, Chiabrando et al., 2011), vegetation monitoring (Sugiura et al., 2005, Laliberte et al., 2011, Hunt et al., 2010), and forest monitoring (Tao et al., 2011, Dandois and Ellis, 2010). However, the drawback is that vision systems, unlike LiDAR, do not have the ability to look through foliage in densely vegetated areas. So, others have investigated LIDAR on small UAVs.

Miller et al. (1998) proposed the first proof-of-concept platform for UAV-based LIDAR and since then several other much more capable small UAV platforms have been developed which address this task (Choi et al., 2009. Nagai et al., 2009, Jaakkola et al., 2010, Lin et al., 2011). Until recently, however, size and budget were significantly larger than most real-world organizations could afford. The UAVs developed by Choi, Nagai, and Jaakkola were very large and used tactical grade inertial measurement units (IMUs) and laser scanners (costing >$50,000 typically). Two LIDAR UAV platforms that use lower cost components include those developed by Serrano (2012) and Wallace et al. (2012). We now describe those in more detail.

Serrano's (2012) work on culvert inspection and Wallace's (2012) work in taking forest inventory are perhaps the most advanced LiDAR-based small UAV systems. Each system used a multicopter platform (e.g., quadcopter or hexacopter). Serrano's system is based on the Ascending Technologies Pelican platform, as seen in Figure 2.2.3 A. Their 3-D point cloud is built by fusing together information from an IMU, an onboard GPS receiver, and a Hokuyo UTM-30LX LIDAR sensor (the same sensor used in our demonstration system). The 3-D point cloud data of the culvert is post-processed by using the IMU / GPS sensor for rough position and pose estimation together with a scan matching algorithm which matches up two consecutive laser scans with the assumption that the objects viewed have not changed or moved in the fraction of a second between scans. Although Serrano's work is theoretically exciting, the results are inconclusive in how well the system could be used for culvert inspection. The conclusion of the thesis indicates that "it would be possible to use the LiDAR to construct a point cloud of the 3-D shape of the (culvert) opening." (Note that this work was partially supervised by the

Massachusetts Institute of Technology's Lincoln Laboratory; hence, there may be Department of Defense classification issues in reporting real-world results.)

Figure 2.2.3 A: Ascending Technologies Pelican.

In Wallace's (2012) system, they developed a sensor package for an octocopter (eight-bladed UAV) that fused an IMU, a GPS, and a high definition (HD) camera (Figure 2.2.3 B). The IMU / GPS system measured rough position and pose estimates while the camera was used with structure-from-motion algorithms to detect the horizontal (and vertical, to a degree) motions of the platforms. Their system did not use a scan matching algorithm to further reduce the error of the 3-D point cloud estimation. However, they were able to show that the inclusion of video information reduced horizontal accuracy from 2 feet to 1.11 feet (root-mean-square (RMS) error). The standard deviation of tree height, as estimated by their system, was 0.85 feet, with a data density of 8 points per 10.76 square feet (1 square meter). 5.90 inch (15 centimeter) accuracy was achievable when more points per tree crown were available. Lastly, the RMS error in tree location was 1.74 feet (0.53 meters), and RMS error in crown width was 2.00 feet (0.61 meters). Figure 2.2.3 C shows an example of the point cloud produced by their method. In summary, this shows that that a LIDAR system on a micro-UAV is able to achieve RMS errors on the order of 3.93 – 19.69 inches (10-50 centimeters) (depending on the measurement) when using a fused IMU/GPS and camera structure-from-motion system.

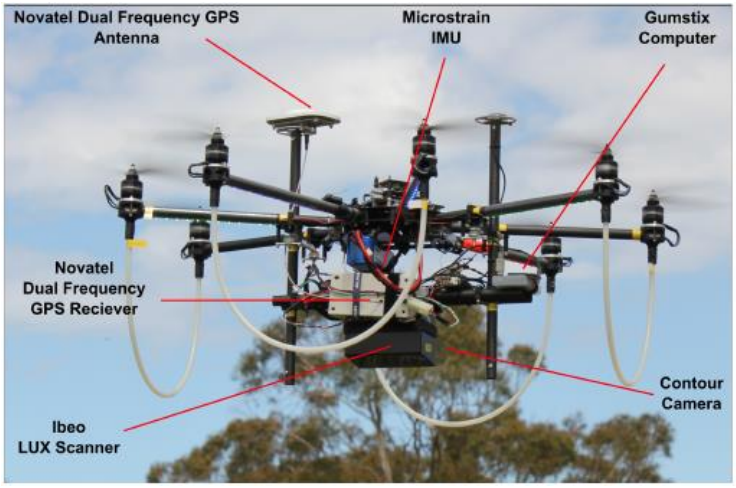

Figure 2.2.3 B: Wallace et al. (2012) forest inventory optocopter platform.

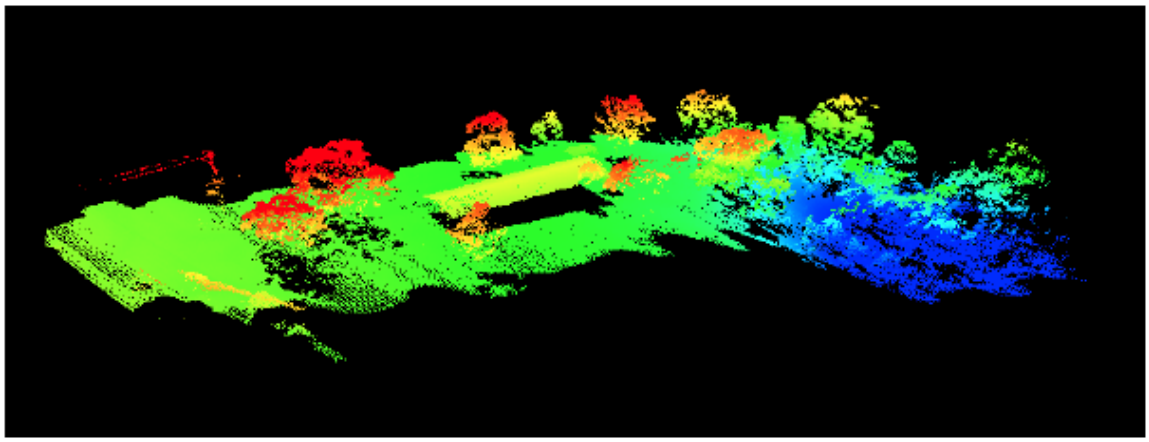

Figure 2.2.3 C: An example point cloud produced by Wallace et al. (2012).

Michigan Tech UAV Sensor-Fused LiDAR Package

To show the feasibility of using small UAV-based LiDAR for transportation purposes, we developed a custom sensor package for a Bergen hexacopter, one of which is also located on the Michigan Tech main campus where the LiDAR testing was developed. The remote sensing package is mounted on the hexacopter as shown in Figure 2.2.3 D. No modifications were made to the airframe or the flight controller for this project; hence, any similar stock small UAV could be used to carry our sensor package, which we now describe in detail.

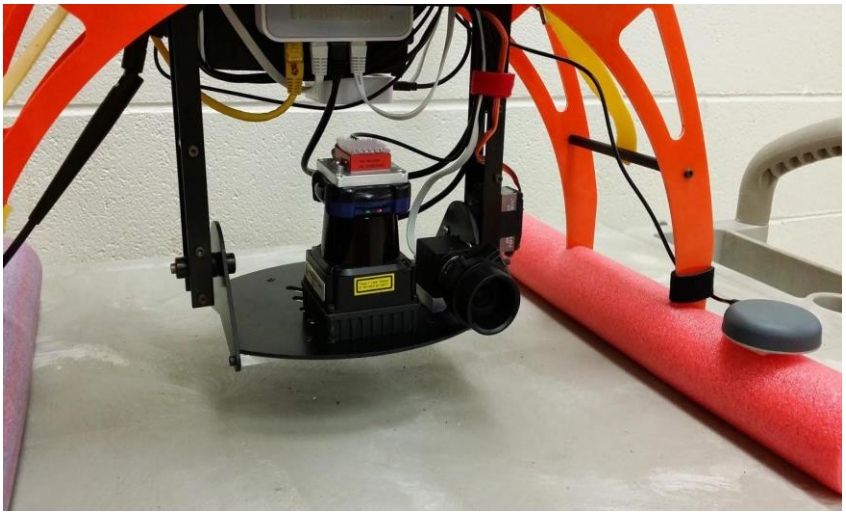

Figure 2.2.3 D: Primary sensors: LiDAR (center, with yellow sticker), VectorNAV inertial navigation sensor (center, red), Point Grey camera (right).

The sensing package is made up of four major components: a Hokuyo UTM-30LX-EW scanning 2-D LiDAR, a VectorNav VN-200 inertial navigation sensor (INS), a Point Grey BFLY-PGE-13S2C-CS Camera, and an Nvidia Jetson TK1 embedded computer system. Additional minor components include two generic LM2596-based DC/DC step-down voltage regulators, a generic 14.8V-2200 milliampere hour lithium ion battery pack, a 5 port network switch, and a TP-Link micro wireless access point. The sensing package operates independently of the small UAV platform and is easily adapted to other micro-UAV systems, or as a hand-held sensing package, or on a ground vehicle such as an automobile or mobile robot. Three items were fabricated using a 3D printer as part of this package: a case for the embedded computer, a mounting bracket for attaching the INS to the LIDAR, and an adapter for mounting the camera to the micro-UAV (Figure 2.2.3 E).

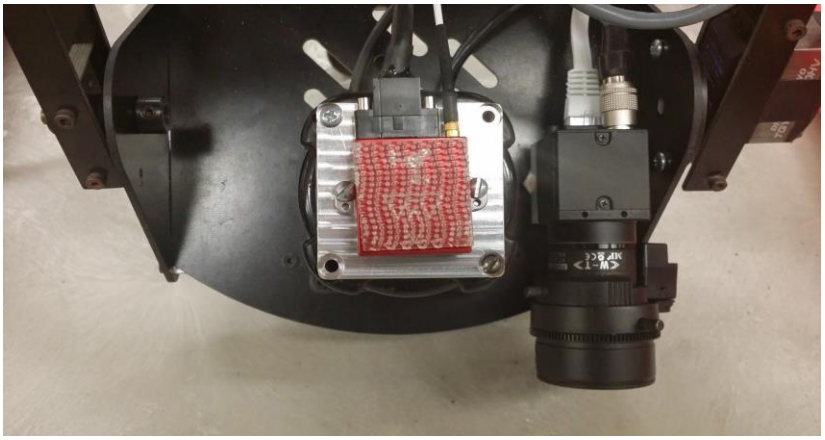

Figure 2.2.3 E: Top view of the primary sensors – LiDAR (silver top) and INS (red) in center; camera at right.

The Hokuyo UTM-30LX-EW LiDAR is capable of scanning 270 degrees in 0.25 degree increments outward to 98.42 feet (30 meters) at a rate of 40Hz. It weighs less than 0.50 pounds (226.80 grams) and has a compact volume of 2.44 inches ×2.44 inches ×3.44 inches, both of which are critical for small UAV applications. This sensor is regarded as a high performance sensor; there are currently no known competing sensors at similar size, weight, and price range which can provide a comparable level of detail. The sensor uses an Ethernet interface to stream data to the embedded computer where data is stored for offline processing. Power is provided directly from a DC/DC step down regulator at 12 volts. The LiDAR sensor is also capable of returning three separate echoes and intensities of each return. These extra data could be useful for identifying foliage and identifying different types of surface materials or defects.

The VectorNav VN-200 integrates a GPS receiver and an IMU in a single package and fuses the data together with a Kalman filter to provide position estimates at a rate of 100 Hertzs. The sensor's IMU contains a MEMS 3-axis gyroscope, 3-axis accelerometer, 3-axis magnetometer, and a barometer (pressure sensor). The default firmware does not use the barometer as an input to the Kalman filter, which is important for micro-UAV applications because of the pressure differential around the vehicle, which is created by the rotors. The sensor is USB-powered and streams data to an RS232 serial port on the Jetson embedded computer. The sensor has a second data interface available for increased sensor data bandwidth, which is not currently used. The sensor requires motion for an accurate position lock; thus, hovering in the same area for an extended period of time will degrade the position estimate. During motion it was found to have excellent performance for both latitude and longitude position estimates.

The Point Grey Black Fly camera is a 1.3 megapixel color camera capable of 22 frames per second (FPS) image capture with a global shutter. We currently are using a 100 megabytes per second Ethernet switch which limits the frame rate to 8 frames per second, but are looking for options that would allow us to mount a GigE network switch on the UAV for utilizing the full 22 frames per second frame rate. The global shutter option captures all of the pixels for each frame at the same time rather than scanning the image one line at a time which is important for UAV applications as to avoid "tearing" of the image during motion. The camera streams data to the embedded computer where the image data is stored for post-processing in an uncompressed format. The camera streams raw, uncompressed image data without any internal filtering, which allows for more advanced image processing algorithms to process the image data at the lowest level offline. However, this utilizes a high amount of communication and storage bandwidth compared to a camera with onboard compression and filtering; a 10 minute flight will often generate more than 30 gigabytes of image data.

The Nvidia Jetson TK1 embedded computer system is mounted in a custom, 3-D printed enclosure mounted on the rear of the UAV as shown in Figure 2.2.3 F. The embedded computer

uses a quad core A15 Arm processor with integrated Nvidia Kepler GPU and 2 gigabytes of on board RAM. The operating system (OS) is executed from an internal 16 gigabytes eMMC storage device; the data logging software and recorded data is saved to an onboard 240 gigabyte solid-state hard drive. The system runs an Ubuntu-based (Linux) OS, and has a full graphics and command line interface which is accessible over a wireless link provided by the TP-Link micro wireless access point (white box mounted on the bottom of the embedded system enclosure). The embedded computer has an array of GPIO connections that could be connected to each of the three sensors to produce significantly more accurate timestamps for synchronizing the data between each sensor. These signals are not currently connected, but the current accuracy of the timestamps appears to be sufficient for our current needs. Additionally, the GPIO pins could be wired to buttons so that data logging could be started and stopped without the need of a laptop and knowledge of the Linux command line system.

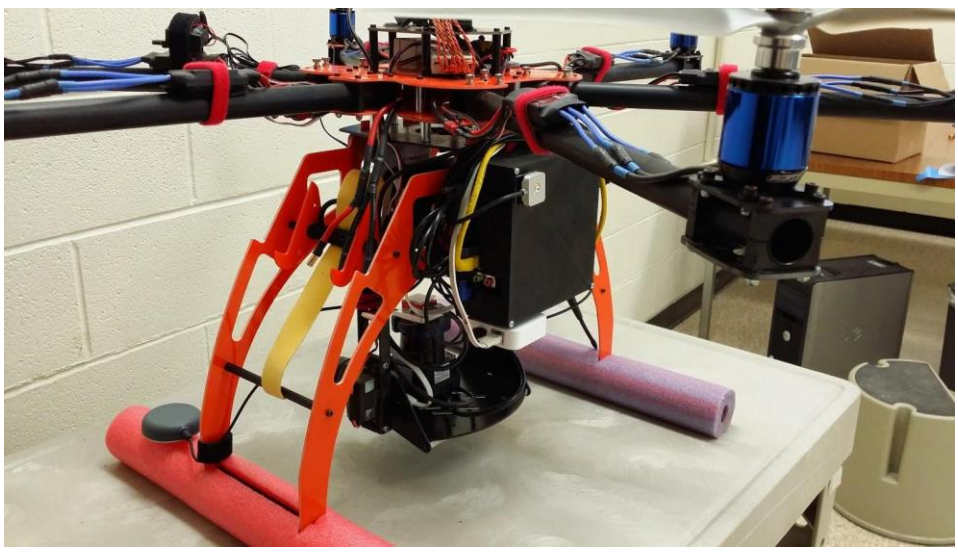

Figure 2.2.3 F: Nvidia Jetson embedded computer system enclosure (black) on rear of hexacopter UAV.

The embedded computer's primary function is to record sensor data. The camera and LiDAR connect via Ethernet as shown in Figure 2.2.3 G. The VectorNav INS connects via RS-232 serial. The embedded computer also provides power to the INS and Wi-Fi access point via USB, which eliminates the need for a dedicated 5 volt DC/DC converter onboard the micro-UAV, as shown in the power diagram in Figure 2.2.3 H. The embedded system has a dedicated DC/DC convertor to meet current draw demands, but a dedicated 5V DC/DC converter could be included if a larger current draw was required.

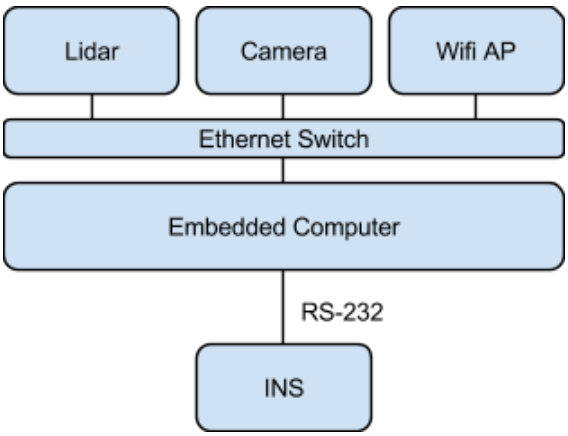

Figure 2.2.3 G: Communication block diagram.

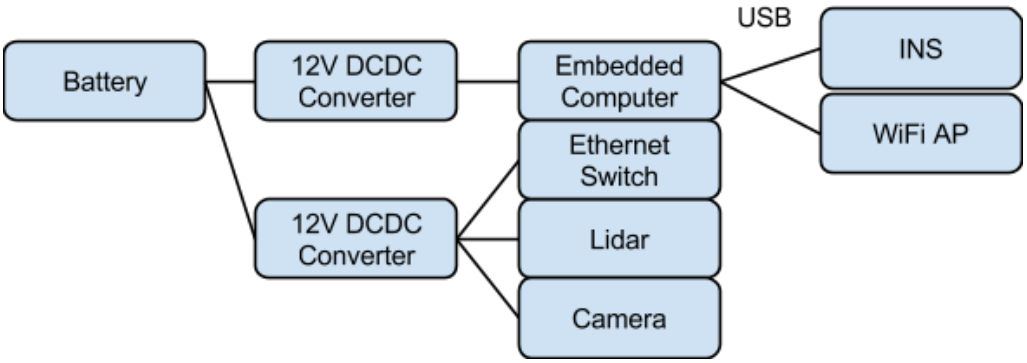

Figure 2.2.3 G: Power Connections.

The main cost elements of this custom sensor package are the Hokuyo LiDAR at ~$5,500, the VectorNAV VN-200 INS at ~$2,900, the PtGrey camera at ~$400, and the Nvidia Jetson at ~$200. Other components add an approximate total cost of $200-300. Hence, the total hardware cost of our sensor package is ~$9,300.

Hokuyo UTM-30LX-EW, http://www.hokuyo-aut.jp/02sensor/07scanner/utm_30lx_ew.html
VectorNav VN-200, http://www.vectornav.com/products/vn200-rugged
Point Grey BlackFly, http://blackfly.ptgrey.com/GIGE/Blackfly
Nvidia Jetson TK1, https://developer.nvidia.com/jetson-tk1

LiDAR Sensor Package Data Logger Software

The data logger has a total of three parts: the LiDAR data recorder, the VectorNav data recorder, and the camera data recorder. Each of these are controlled by a startup script. This script sets up which of the sensor data is going to be collected. It also stops the collection of the data. The script allows for remote display of all data. Each one of the sensors is controlled by third party libraries provided by the sensor manufacturers. The camera uses the PointGrey

FlyCapture® SDK. The VN-200 uses a library provided by VectorNav, and the LiDAR uses a library, URG Network, provided by Hokuyo Automatic. Both the VectorNav and URG Network libraries are open source.

To run the software, connect to the embedded system at *192.168.0.2* via SSH. Then go to the folder containing the data logging software, currently located at */mnt/ssd/SensorLogger*. Execute the data logger system with *./collectdata*, following the instructions given by the script. After the data collection is complete, enter 0 to exit the script. Data is stored in the data_storage folder. Within that folder is a pics folder, which contains the camera frames, a file called LIDAR_data.csv and LIDAR_info.csv, which contains the LiDAR data, and a file called vn.csv, which contains data from the VectorNav.

The LiDAR data recorder saves the LiDAR points into a comma-separated file in the data directory. Each line of the comma separated values (CSV) file is one scan from the LiDAR. The first column is the system timestamp when the data was received. The second column is the sensor timestamp in microseconds from startup. The remaining columns are the range and intensity values for each measurement in the scan. Each measurement consists of six values: three distance measurements to each detected echo, followed by three intensity values corresponding to each echo. Most measurements consist of one echo, and the other two echoes are zero-valued.

The VectorNav Data Recorder saves the GPS/INS data into a comma-separated file. The data saved consists of a system timestamp of when the data was received, a sensor timestamp in microseconds from startup, the GPS provided timestamp, the orientation of the sensor in quaternion format, and the GPS coordinates. The VectorNav has a variety of options as to what data is sent to the embedded system from the sensor, and we chose to limit the data logging to these values in an effort to maintain a high update rate given the limited sensor bandwidth available over RS232. A second data port is available on the sensor for accessing more data such as the raw IMU sensor data, but this has not been done since the sensor appears to be providing an acceptable position and orientation estimate for our needs at this time.

The Camera Data Recorder grabs images from the camera. It saves each image to a bitmap image file with 8-bit color. Images are given a filename consisting of a sequence number and a system timestamp. This allows for images to be read in proper order during post-processing. Sections 3.1.4 and 3.2.4 describe the processing of the sensor in detail.

FlyCapture® SDK, http://ww2.ptgrey.com/sdk/flycap
VectorNav C/C++ Library, http://www.vectornav.com/support/downloads
URG Network, http://sourceforge.net/projects/urgnetwork/

3. Methodology

The following sections describe the types of infrastructure that our UAVs and sensor were prioritized to sense, based on MDOT input and the work plan, and then follows with the lab testing completed so that effective field demonstrations could be accomplished.

3.1 Transportation Infrastructure

Creating a state-of-the-practice reporting covering the use of UAVs for transportation purposes was the first step in understanding how this type of technology could prove beneficial for MDOT. Through this review, different types of sensors, platforms, and applications that have been proven to work for other UAV applications were noted and applied towards this study. These include optical (visible and near-infrared light), thermal, and LiDAR sensors that are attached to single- and multi-rotor helicopters, tethered devices (balloons and blimps) platforms.

3.1.1 Bridge Inspection

Optical (i.e. visible) imagery use for NDE applications pertaining to bridge decks has been the focus of previous funding from the United States Department of Transportation (US DOT) Office of the Assistant Secretary for Research and Technology (OST-R) (formerly the Research and Innovative Technology Administration, RITA). Using the principles of photogrammetry, the project team successfully inspected bridge elements and calculated bridge distress quantities (e.g. percent spall and crack width). Photogrammetry is "the science or art of deducing the physical dimensions of objects from measurements on photographs of the objects" (Henriksen 1994). It includes the generation of 3-D models from stereo pairs of imagery in order to obtain depth and height information, and is part of the larger field of 3-D optics, and can be referred to as 3-D photogrammetry. Stereo images have to be collected with an approximate 60 percent overlap in order to generate these models (McGlone et al. 2004). The project team's use of 3-D optics/photogrammetry was a technology demonstration to apply a potentially low-cost remote sensing method not typically yet seen in transportation applications. At the distance used in these previous projects, the deployment can be described as an implementation of close range photogrammetry (Luhmann et al. 2007).

Applying photogrammetry methods to remote sensors was made possible by developing platforms such as the easily deployable 3-D Optical Bridge Evaluation System (3DOBS), which captured very high resolution optical imagery (up to 0.5 millimeters; 0.02 inches) at low speeds (less than 10 miles per hour) (Figure 3.1.1 A). 3DOBS collected imagery were processed through close-range photogrammetry software and reconstructed into a 3-D surface model and DEM through the use of Agisoft PhotoScan. ESRI's ArcGIS software could then map the location, volume, and area of spalls that were detected by 3DOBS, providing a critical indicator on the condition of the bridge surface by using a low-cost system (approximately $5,000). Additional

funding, through a separate MDOT research project, enabled 3DOBS to be developed for higher speeds (at least 45 miles per hour) using a Red EPIC high-frame rate, high-resolution camera. Imagery captured and reconstructed into a 3-D model has produced DEMs with 0.5 millimeter resolution. This updated platform and sensor costs approximately $40,000, but can operate at near highway speeds (>= 45 miles per hour / 72 kilometers per hour). As compared to the standard methodology of measuring and mapping bridge distresses, which include hammer sounding or chain drag techniques and closure of the bridge for inspector safety, the remote sensing technologies and platforms provided faster data collection, without the necessity of closing the bridge.

Figure 3.1.1 A: 3DOBS vehicle mount in the bed of a pickup truck.

For the purposes of this analysis, similar sensors were used to analyze bridge elements of two separate bridges in Livonia, Michigan, but operated from a UAV for wider-area data collection. The optical camera placed on the Bergen hexacopter was a 36 megapixel Nikon D800 camera. The optical system is being evaluated to create sub-centimeter 3-D models of bridge decks to help locate problems such as spalls (potholes). Optical imagery area reconstructed in Agisoft PhotoScan and processed to produce a DEM. Further information on these field demonstrations can be found in Section 4.1.1.

Applications of thermal remote sensing to monitor concrete surfaces are mainly aimed to detect anomalies associated to delaminations and similar structural defects (Maser and Roddis 1990; Washer et al. 2009 and 2010; ASTM 2007; and ACI 2001). Detection of such defects, e.g. delaminations, can help infrastructure inspectors to identify damaged areas before they develop from delaminations into spalls (Ahlborn et al. 2012). The basic idea behind such approach is that the concrete surface changes temperature due to changes in the environmental conditions, either due to natural variation, e.g. the diurnal temperature and insolation changes, or due to artificial heat sources, e.g. heaters deployed for testing purposes.

The temperature changes affect differently areas with defects (e.g. delaminations) from intact areas, resulting in temperature differences that can be detected with the thermal remote sensing methods. The areas with defects can be inferred and mapped from the radiance or temperature differences, even if they would otherwise (e.g. via visual inspection) not be noticed.

The spatial distribution of temperatures can be analyzed as a raw radiance map produce by the thermal remote sensing instrument, or it can be further processed to obtain a calibrated surface temperature map; for most purposes a raw radiance map will suffice, as the main goal is to see relative differences in temperature, which will be revealed by either the radiance or true temperature image. Thermal remote sensing instruments usually consist of an array of thermal sensor similar to the CCD or CMOS sensor used in common photographic or video cameras, but sensitive to the thermal infrared part of the spectrum (see Figure 2.2.2 A). Such thermal cameras produce digital images of the surface being monitored, with each pixel of the image representing a radiance or a temperature.

The temperature and associated radiance differences seen in a thermal image arise from the way heat is transferred in and out of the concrete surface, following the fundamental laws of thermodynamics. A concrete surface at a different temperature than the surrounding environment will tend to equilibrate with that environments temperature; if the concrete surface is at a lower temperature than the ambient air (e.g. during the morning as the air is quickly heated by solar radiation), it will start to heat up, raising its temperature in a tendency to equilibrate thermally with the environment. Conversely, if the concrete surface is at a higher temperature than the ambient air (e.g. after sunset as the air quickly cools down), it will start to cool down, lowering its temperature again in a tendency to equilibrate thermally with the environment. In the case just discussed the thermal energy is being transferred by conduction with the air in contact with the concrete (and by convection of the air), but an analogous situation can be considered for the case of thermal energy being transferred by radiation of electromagnetic energy. A surface being exposed to electromagnetic radiation will absorb part of that radiation (e.g. by the direct exposure to solar radiation), increasing its temperature, but it will also radiate energy according to the principles discussed in the previous section, losing energy and tending to cool down (e.g. after sunset). The balance between incident and radiated energy, and the thermal exchange with the surrounding air will determine whether the surface will tend to heat or cool down.

Structural defects and imperfections alter the heat transfer patters (Maldague, 1993; Starnes, 2002; Washer, 2009). A delamination, which is basically a void in the concrete filled either with air or water, will conduct heat differently from the rest of the concrete structure. As the concrete temperature increases from the surface inwards (e.g. after sunrise), a delamination

will act as a barrier slowing down heat transfer into the deeper parts of the concrete structure, this slowdown in heat transfer will result in an increase of the temperature of the concrete above the delamination. This is illustrated in Figure 3.1.1 B, where the area above the delamination accumulates the heat that cannot be transferred to the deeper parts of the concrete body, resulting in a higher surface temperature.

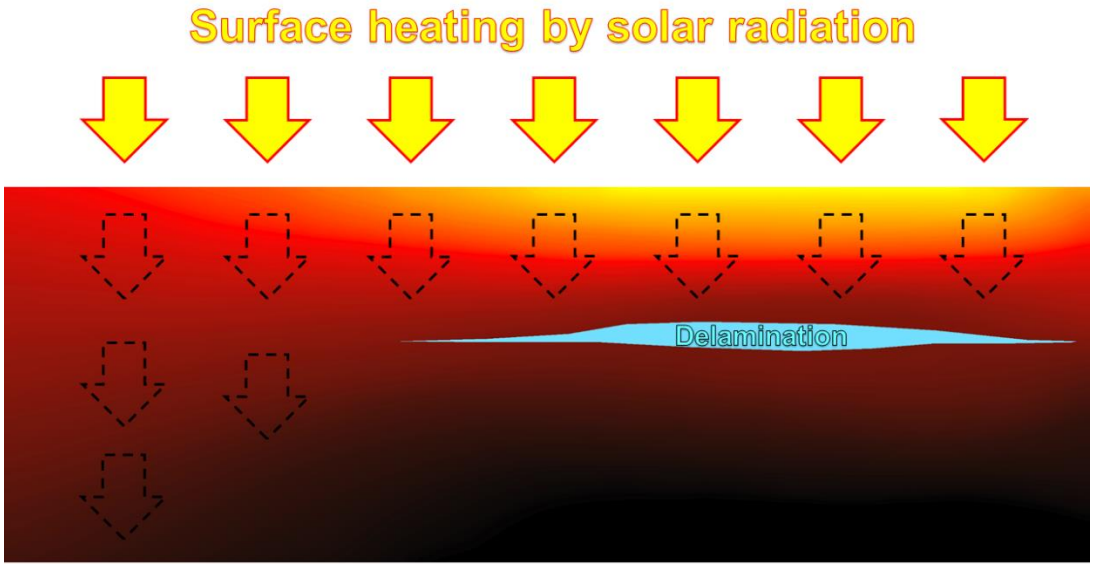

Figure 3.1.1 B: Cross section illustration of heat flow through solid (left side) and delaminated (right) concrete. For a concrete body heated from its surface (e.g. through solar radiation) the heat flow will start to move away from the surface and through the body's interior. In the presence of a delamination the heat flow is interrupted or slowed down, leading to an increase of temperature right above the delamination.

When applied to concrete surfaces, the principles of thermal remote sensing follows the discussion from the previous section, and the values of the concrete emissivity and atmospheric absorption become critical in calculating radiance, temperature, and emissive power. Thermal remote sensing instruments usually work in the "thermal infrared atmospheric windows" discussed in the previous section, where the absorption is minimal, and can be modeled by taking into account and modeling the absorption of the most critical gases present in the atmosphere (e.g. water vapor). The absorption will depend on the amount of atmosphere (and therefore absorbing gases) between the emitting surface and the sensor: the longer the distance the stronger the absorption, applying the remote sensing technique over longer distances produces higher absorption and lower quality data. Working in high humidity environments also reduces the data quality, and obviously the quality and even feasibility of obtaining data depends as well on the presence of other potential atmospheric blocking conditions (e.g. fog, dust, smoke, etc.). On-site applications of thermal monitoring to concrete surfaces are usually affected only little by atmospheric absorption if atmospheric conditions are good, due to the short distance (usually from meters to tens of meters) between the concrete

surface and monitoring instrument, and these effects are often taken into account when calculating the emitted radiance from the surface. Longer distance applications of the thermal monitoring methods may face more challenges in that respect.

Practical applications of thermal remote sensing include both passive and active heat sources (Alqennah, 2000). Passive thermal remote sensing uses natural heat source, mainly solar heating, whereas active methods use artificial sources, like heat lamps and other heating devices. In both cases it is necessary to have variations of the heating over time to allow for differences in heat transfer to highlight the anomalies (e.g. associated to delaminations); in the passive case the diurnal variation associated to insolation (from sunrise to sunset) provides that temperature change, and in the active case it depends on the time and mode of exposure to the heat source.

Asphalt and concrete pavement emissivity is usually assumed to be high (> 0.9), but this value can vary depending on the specific properties of the asphalt or concrete surface (e.g. how rough or smooth it is). More importantly from a practical standpoint is the possibility that other substances covering the concrete can dramatically change the surface emissivity, leading to very large differences in the calculated temperature (e.g. Clark et al. 2003). Although it may have an important impact on temperature measurements, emissivity may not be a critical variable in some cases where only relative differences of temperature (and therefore of radiance) are important, as long as the whole surface being measured has the same emissivity. Also important are other environmental variables that also control the heat transfer, like wind speed, which enhances convective and advective heat transfer (Washer et al. 2009; ASTM 2007).

Besides the characteristics of the concrete, surface material covering the concrete, and atmosphere, it is also important to consider the conditions of the potential defects that are attempted to be detected by the monitoring. The substance filling a delamination can have a large effect on heat transfer and therefore on potential detectability by thermal remotes sensing; for instance water will conduct heat much better than air (even at a similar rate than concrete), and therefore a water filled delamination may be much harder to detect by thermal methods (Maser and Roddis, 1990). The depth and width of the delaminations also play a key role in how heat is transferred to the surface, with deeper and thinner delaminations being harder to detect (Alqennah, 2000; Vaghefi et al. 2013). Finally, for passive thermal remote sensing the time of the day when the monitoring is done, and the relationship to the insolation (the amount of solar radiation received by the surface) are also important. For instance, the highest thermal contrast will be achieved at different times for delaminations at different depths, with deeper delaminations taking as much seven hours to achieve maximum contrast (Washer et al. 2009).

Thermal remote sensing is seen as advantageous because it is a relatively fast and undisruptive monitoring technique that translates in shorter inspection and lane closure times (Maser and Roddis, 1990). The digital format of the thermal remote sensing instruments output allows to easily combine and integrate the monitoring information with other data platforms, including standard GIS software packages, allowing to store the monitoring data in a georeferenced database (Ahlborn et al. 2012).

3.1.2 Confined Space

Confined spaces inspection which includes pump stations and culverts are not considered to be a traditional use for UAVs. But with advances in technology, there are UAVs small enough to be flown into these locations. Larger traditional UAVs like the Bergen hexacopters are too large to be flown into buildings or other structures so other smaller UAVs need to be utilized.

Pump stations along freeways can be hazardous to inspectors after major storm events or power outages (Figure 3.1.2 A). An example of these types of events would be the flooding of the Detroit area freeways during storm events in August 2014. A small UAV has the capability of flying into a pump station while transmitting video back to the inspector without the inspector entering. Micro UAVs are small enough to fly through doorways, hatches and other small openings (Figure 3.1.2 B). These UAVs are typically less than $200 and if lost in a pump station are easily replaced. They would also help keep inspectors safe as they would not have to enter into the stations without knowing what conditions are first.

Figure 3.1.2 A: Dallas pump station along I-75.

Figure 3.1.2 B: Example of a hatch that a UAV would have to fly through.

3.1.3 Traffic Monitoring

There has been much discussion about using UAVs for traffic monitoring, whether for short term assessment of conditions at a crash scene or an intersection, or longer term monitoring of a construction zone or other priority area. Different kinds of UAVs are best suited for different applications; the challenge can be selecting the right aircraft/sensor package for the job.

Traditional traffic monitoring cameras are mounted on masts near intersections or stretches of highway that are known to be congested. While useful, these cameras require the installation of masts to support the cameras and network infrastructure to transmit the signal to a traffic operations center (TOC), not to mention legacy operations and maintenance issues. Blimps/aerostats (or other types of UAVs) can provide a persistent observation platform where traffic monitoring cameras would be useful but the time and cost to install the cameras is prohibitive or not desired on a long-term basis.

Construction zones and large sporting events are two cases where traffic monitoring cameras can prove useful to managing traffic flow (Figure 3.1.3 A). Aerostats and other types of UAVs can provide temporary, persistent monitoring of intersections or highway corridors that require monitoring but do not have the infrastructure for traffic cameras in place. Camera mast heights vary but generally they can be up to 60 feet high. The altitude of the blimp and the focal length of the camera lens can be adjusted to optimize the field of view for each deployment site (Figure 3.1.3 B).

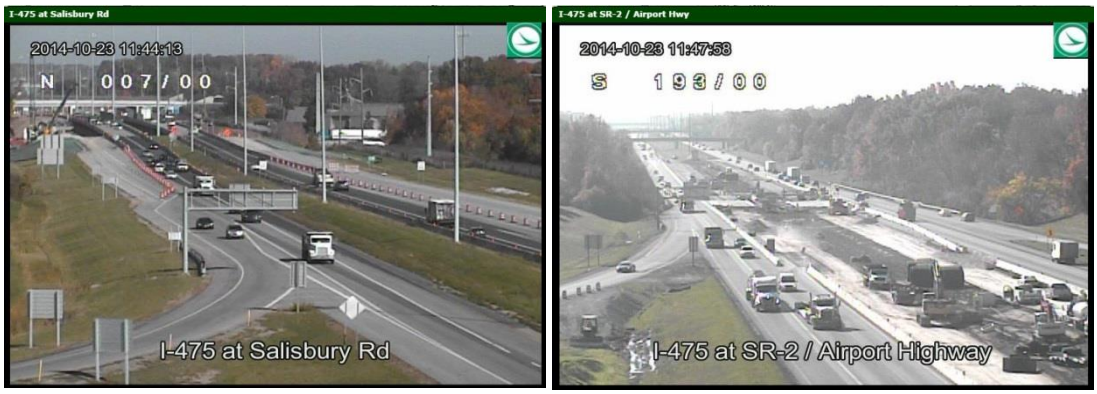

Figure 3.1.3 A: Two views from traffic cameras on I-475 in Toledo, OH, which monitor traffic through a construction zone.

Figure 3.1.3 B: Views of US 23 and Plymouth Road (left and center) from the MTRI blimp (altitude approximately 120 feet) during a lab test flight, and construction site traffic monitoring at the Interstate-96 site using a quadcopter (right).

3.1.4 Roadway Assets

We developed and tested a computer vision method for detecting and tracking specific roadway assets from the UAV. The sensor used for this work was an HD camera connected to an on-board computer for processing and data logging. The algorithm we developed is able to detect and track road signs by using a set of training images of the type of sign to track. The computer learns how to find and track the type of sign by automatically learning the image features that comprise the sign. The tracker is generalized such that any type of roadway assets could be detected and tracked; e.g., different types of signs and indicators, guard rails, and lamps.

The algorithm is mainly composed of two parts:

1. Detection:

The Viola-Jones classifier is utilized for the purpose of detecting desired objects within an image (video frame). This classifier is a cascade of several weak classifiers that work together,

providing very good performance in terms of detection and false positive rates, and have the possibility of real time processing.

2. Tracking:

Several tracking algorithms were also tested alongside the Viola-Jones classifier. The algorithms under investigation are:

- Kanade-Lucas-Tomasi (KLT) tracker. (feature based)
- Histogram based tracker.
- Scale-Invariant Feature Transform (SIFT) based tracker. (feature based)
- Speeded Up Robust Features (SURF) based tracker. (feature based)
- BRISK based tracker. (feature based)

These tracking algorithms are able to track a detected piece of road side asset throughout successive images. This is useful for purposes such as counting different types of signs in a video sequence.

Algorithm

A flowchart for the object detection and tracking is illustrated in Figure 3.1.4 A. Video is processed frame-by-frame. First, selected road side asset objects are detected. Second, feature points on the detected object are collected. Then, these points are tracked throughout the video sequence.

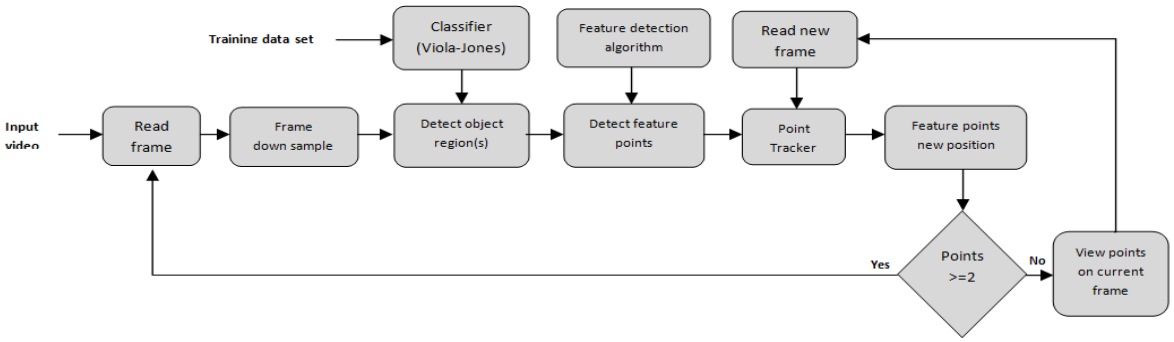

Figure 3.1.4 A: Road side asset detection and tracking algorithm flowchart

Remarks:

- The process of training the Viola-Jones classifier is done prior to running the algorithm, since it is not a real time process. The classifier uses pre-collected example images of the type of road side asset that one wishes to detect and track. Hence, in order to use this method, one only has to provide example images (such as those taken with a cell-phone camera); the classifier does the rest.

- Once the classifier detect the object(s) at a given frame, a feature extraction method (e.g. SIFT) is applied for tracking purposes in the following frames, which allows the algorithm to have a faster performance.
- The point tracker uses the feature points in a succession of two frames to compute the geometric transformation of the tracked object.
- If, at a given frame, the number of feature points of an object falls below a given threshold, the classifier initiates a new search for that object starting from the current frame.
- The purpose of the down-sampling step is to skip the processing of frames where objects are expected not to show up based on previous frames. This can improve the average processing time of each frame.

For the purpose of demonstration, the algorithm was tested on three different types of roadway assets: a stop sign, a handicap parking sign, and a traffic light. Figure 3.1.4 B shows examples of how the algorithm is able to detect these roadway assets in example images.

Figure 3.1.4 C and Figure 3.1.4 D provides an illustration of tracking of different road signs. The '+' signs, within the box surrounding the detected object are the positions of the detected features. The KLT tracker was used to generate these results.

Figure 3.1.4 B: Examples of road side asset detection in imagery.

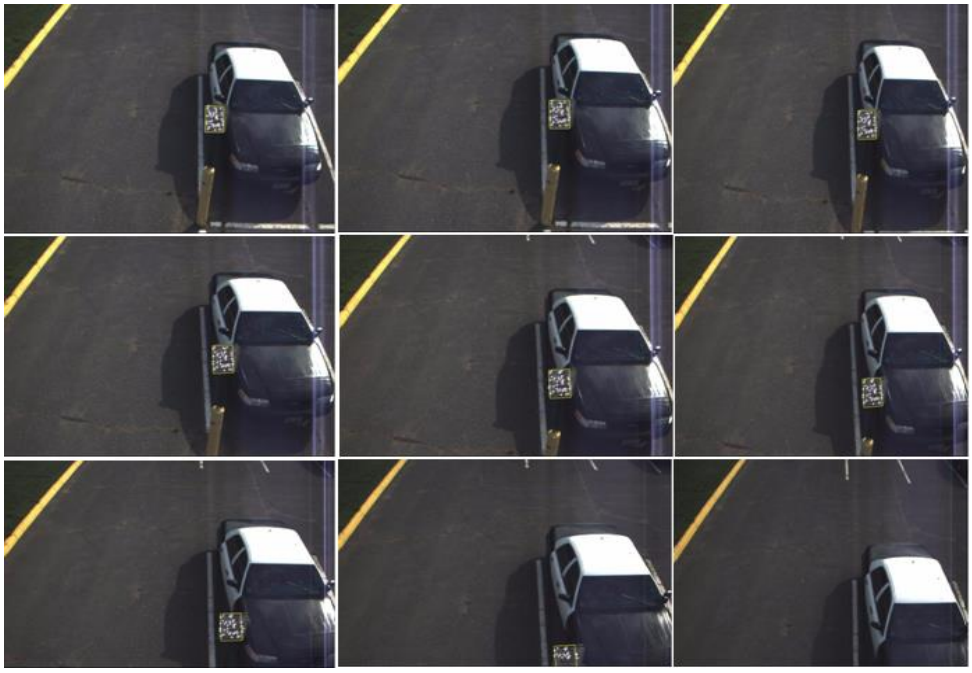

Figure 3.1.4 C: Detection and tracking a No-Parking sign from above from the UAV.

Figure 3.1.4 D: Detection and tracking a No Parking warning sign from side view from UAV.

3.2 Lab Testing

3.2.1 Bridge Inspection

Due to prior in-depth experience in using photogrammetry to create orthoimagery, DEMs, and 3-D hillshades to aid in the detection and quantification of distress features on bridge decks, further lab testing was not required. Lab testing during previously funded projects aided in determining specific requirements of the camera, sensor, platforms, and image resolutions. This section reviews lab tests conducted during the initial phases of the US DOT Office of the Assistant Secretary for Research and Technology (formally Research and Innovative Technology Administration) bridge condition project (Contract #: DTOS59-10-H-00001).

Various experiments were performed to test the cameras and software limitations using a piece of foam board, which was used for its ease to shape and attach extra pieces. A wedge shape was carved into the board that allowed for the determination the horizontal resolution of the program, which relates to the width of cracks on bridges. Pieces of cardboard were arranged in a stair-step fashion that shows the programs limit to resolve height or depth measurements. Finally, different colored spheres were added to show if there would be problems with generating accurate models due to poor contrast and the different sizes show what the resolution is with respect to generating rounded features. All of the tests produced similar results and demonstrated that photos can be taken throughout daylight hours without concern over reducing resolution or accuracy. Figure 3.2.1 A is an example of one of the photos taken of the foam board and Figure 3.2.1 B is an example of the 3D model created with PhotoScan from the stereo overlapping digital photographs.

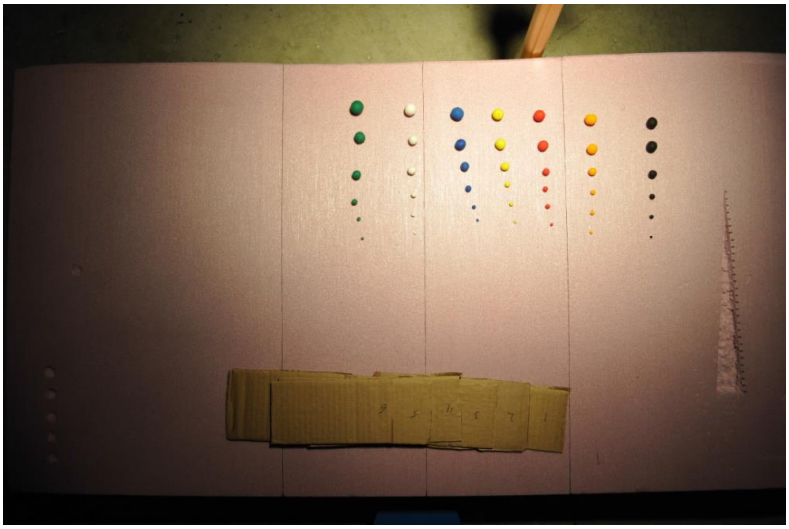

Figure 3.2.1 A: Photo taken of the foam board used to determine the restrictions of AgiSoft Photoscan.

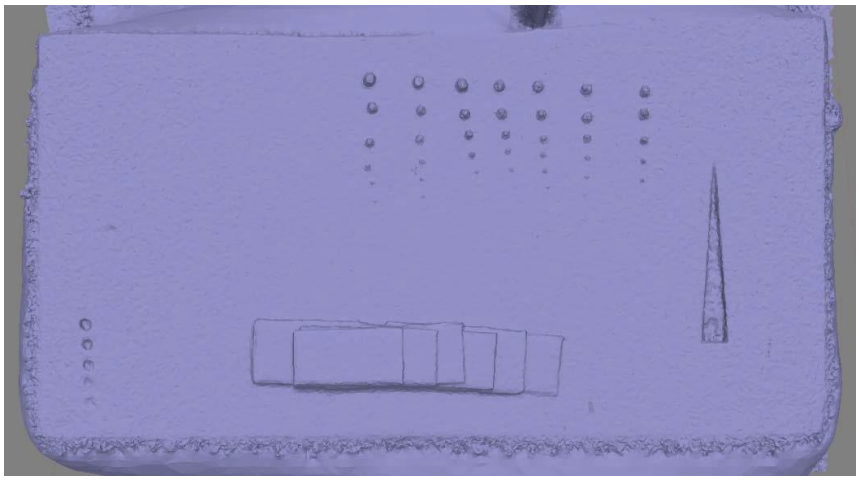

Figure 3.2.1 B: The resulting AgiSoft Photoscan model. A total of five images were used to generate the model.

Additional tests were conducted to consider how the quantity of photos affected the model. Results indicated that increasing the number of photos and coverage, noise was reduced and a clearer, more accurate model was produced. Following these lab tests and results, in field testing was conducted near Ann Arbor, Michigan and the vehicle mount seen in Figure 3.1.1 A was built. The selected camera, a Nikon D5000 was placed 9 feet above the bridge deck and the vehicle was driven across the bridge at a speed of 1 mile per hour, ensuring 60 percent overlap between photos. These photos were placed into AgiSoft Photoscan and reconstructed to create an orthophoto, which was georeferenced to an image of the bridge by using known GPS points and markers. Final outputs based on lab tests and in-field demonstrations can be seen in Figure 3.2.1 C.

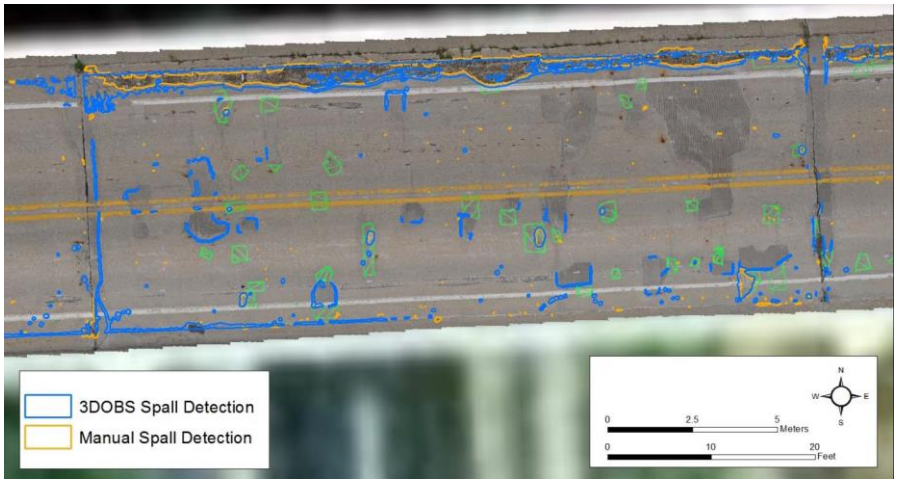

Figure 3.2.1 C: The reconstructed orthophoto of Willow Road Bridge near Milan, Michigan and the detected spalls based on manual interpretation and automated detection.

3.2.2 Confined Space

Four UAVs were tested from use in confined spaces. These include the DJI Phantom, Heli-Max 1 Si, Walkera QR 100S and the Blackout Mini H Quad. All of these have different capabilities and are of different sizes. They all had the ability to capture pictures and video which would be useful for confined space inspection.

The DJI Phantom 1 was the first UAV to be tested for confined spaces. Because of its small size (13.8 inches x 13.8 inches x 7.5 inches) it was more suited to confined spaces. Testing was first done in the lab at MTRI as shown in Figure 3.2.2 A. The first generation Phantom carried a GoPro Hero 3 camera to record video or to capture pictures (Figure 3.2.2 B). An FPV (first person viewer) was also added so that the pilot could fly it through into confined spaces out of line of sight.

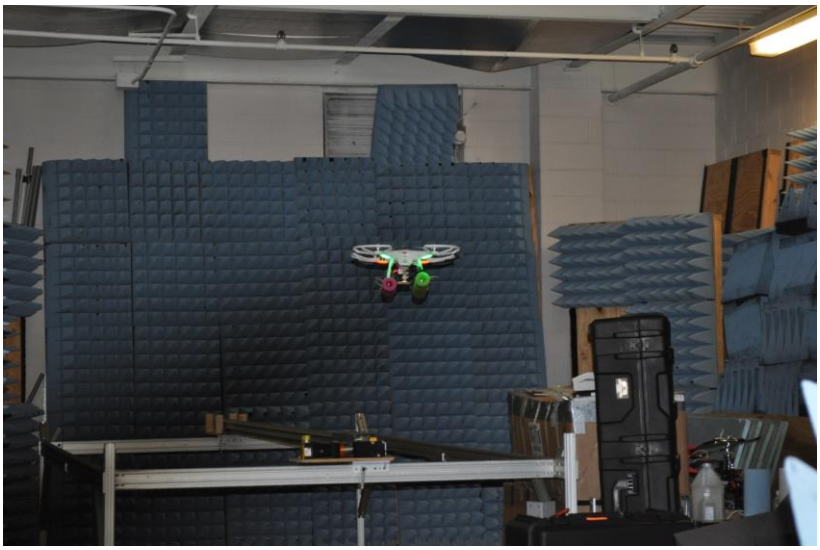

Figure 3.2.2 A: DJI Phantom testing in a confined space in the lab at MTRI.

Figure 3.2.2 B: Extracted frame from the GoPro video captured from the lab testing of the Phantom 1.

Successful in lab testing led to a field test of the Phantom 1 within a pump station. These initial tests were performed with the Phantom taking off, flying and landing in the lower level of the pump station as these test were better understand the limitations of flying a UAV in these locations (Figures 3.2.2 C and 3.2.2 D). As with the earlier tests in the MTRI lab, an FPV was attached to the Phantom. Video of the flights was taken using the GoPro mounted underneath and the frames were extracted (Figure 3.2.2 E).

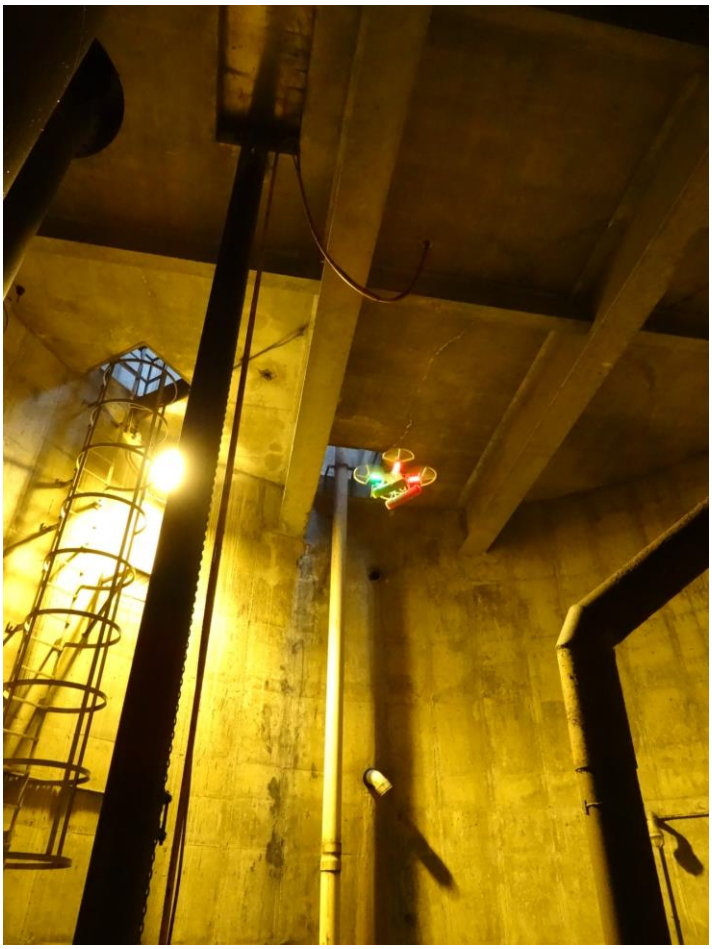

Figure 3.2.2 C: DJI Phantom flying in a pump station.

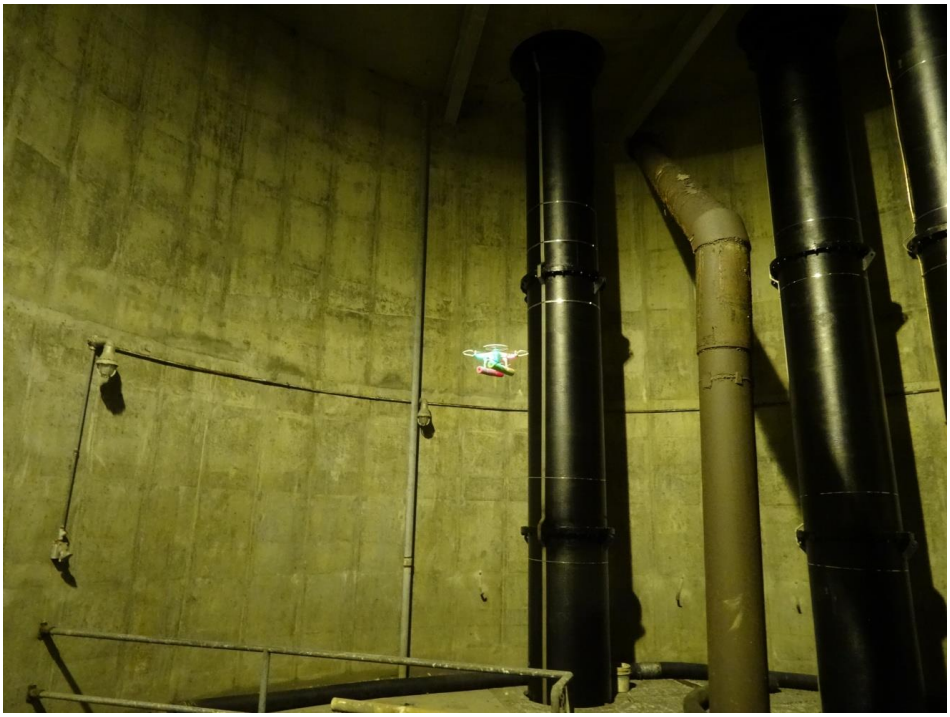

Figure 3.2.2 D: DJI Phantom flying in a pump station.

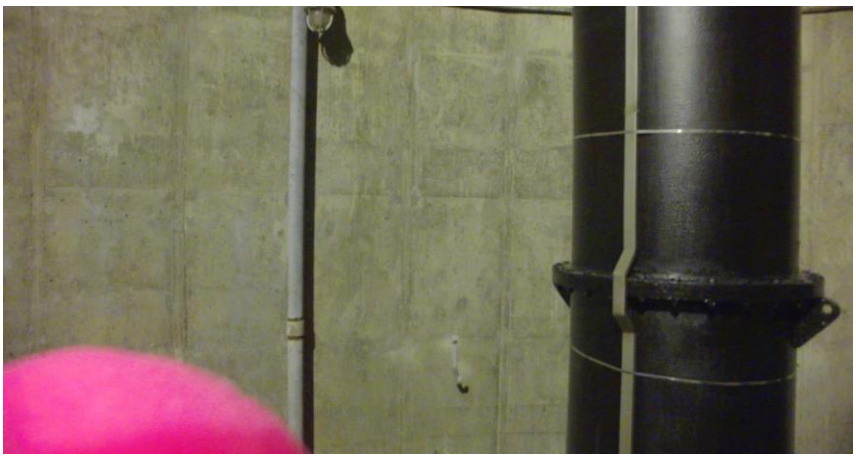

Figure 3.2.2 E: Extracted frame from the video captured from the DJI Phantom.

Flying in a confined space with the Phantom, though it proved successful, was challenging. Any air currents or turbulence within the confined space would move the Phantom in unexpected directs and had to be quickly compensated for as there is very little space for maneuvering. The Phantom also needed to be at least two feet away from any walls or large objects. If the Phantom were closer, the air being pushed down by the props would create vortices that would pull it into the wall or object. While the Phantom is a stable platform and was successful, these test showed to the project team that a smaller UAV would be more practical for confined spaces.

Micro-quadcopters like the Heli-Max 1Si and the Walkera QR 100S are smaller UAVs that would be more practical for confined spaces. They are less than half the size of the Phantom and cost less than $200 where the Phantom 1 cost over $400. Both UAVs were tested in MTRI's lab (Figure 3.2.2 F) to make sure they were able to be flown. These tests also included taking pictures and video to compare the quality with the GoPro (Figure 3.2.2 G). The smaller size allowed for both UAVs to be able to get closer to walls and other obstacles before vortices form.

Figure 3.2.2 F: Test the Heli-Max 1Si in the MTRI Lab.

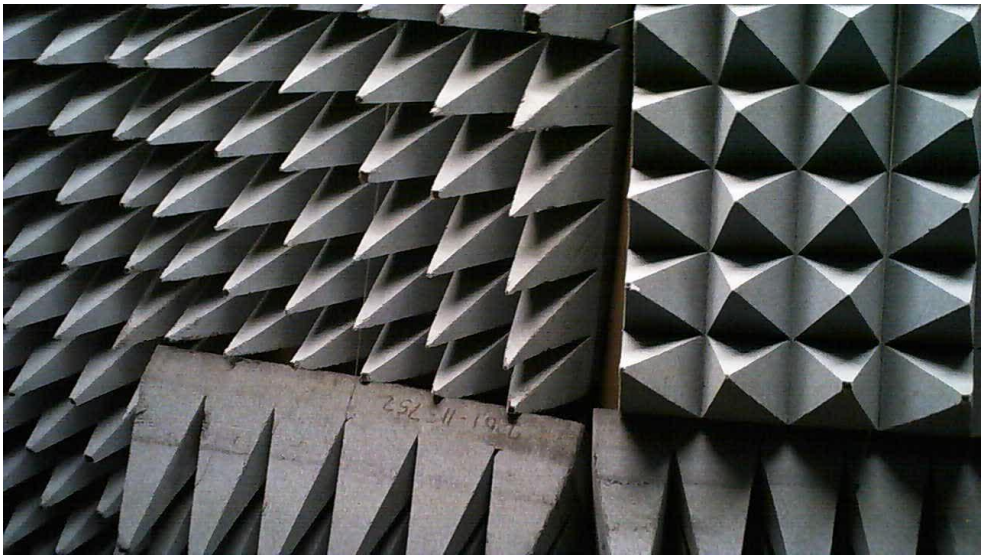

Figure 3.2.2 G: Extracted frame captured by the Heli-Max 1Si during the lab testing.

Another confined space that was being investigated was culverts. The Blackout mini H Quad was selected due to its small size and maneuverability with reasonable price (currently $460). This system is sold as a kit and is completely customizable. For our purposes, an FPV camera was installed which also records the video onboard. This setup would help the pilot through the culvert while it is out of line of sight as well as collect the video for review later. For lab testing, a section of culvert that was 6 feet long and 4 feet wide was supplied by the Road Commission for Oakland County (RCOC). The Blackout was flown through the culvert collecting video as shown in Figures 3.2.2 H and 3.2.2 I.

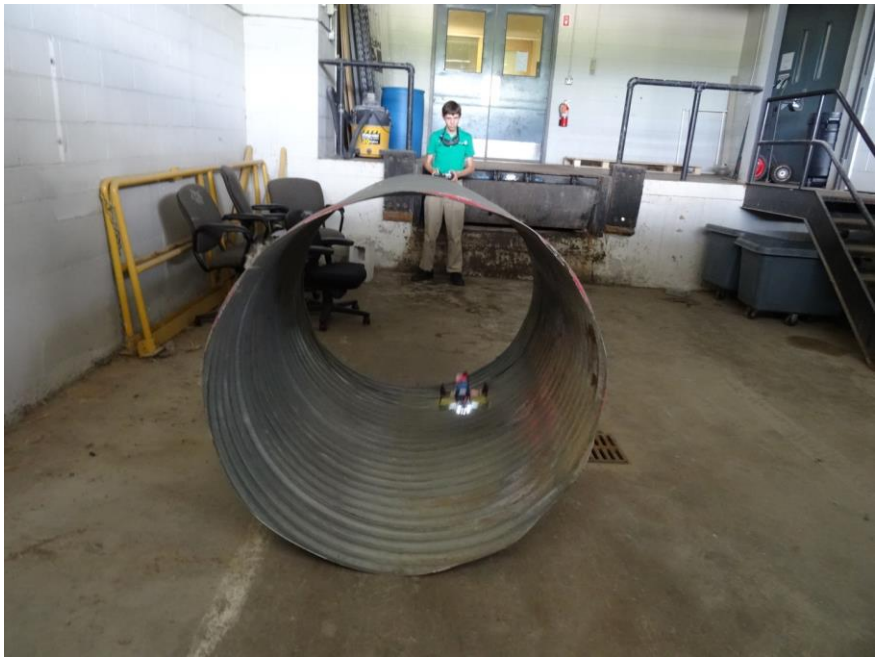

Figure 3.2.2 H: The Blackout Mini H quad being flown through a section of culvert.

Figure 3.2.2 I: An extracted frame from the Blackout while flying through a culvert section. This shows the interior wall of the culvert as the UAV was hovering and turning inside the section.